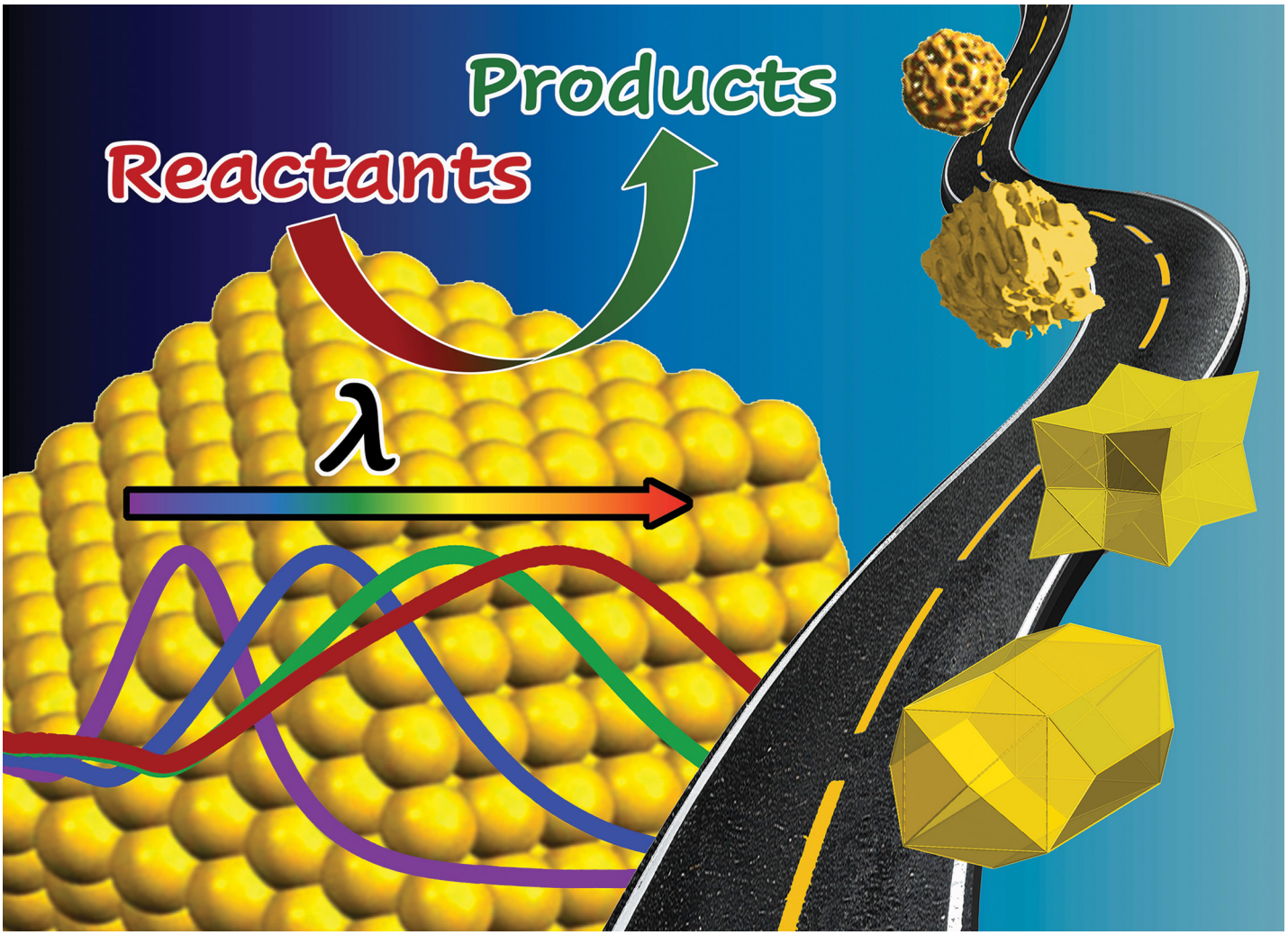


**Showcasing research from Professor Hui Wang's laboratory, Department of Chemistry and Biochemistry, University of South Carolina, Columbia, South Carolina, United States of America.**

A repertoire of gold-based nanostructures with integrated optical and catalytic tunabilities

This Feature Article elaborates on strategies for integrating optical and catalytic tunabilities in deliberately designed and experimentally realizable gold-based nanostructures.

Image reproduced by permission of Hui Wang from *Chem. Commun.*, 2025, **61**, 13807.

## As featured in:


See Hui Wang,
*Chem. Commun.*, 2025, **61**, 13807.

ROYAL SOCIETY OF CHEMISTRY

rsc.li/chemcomm

Registered charity number: 207890

ChemComm

ROYAL SOCIETY OF CHEMISTRY

FEATURE ARTICLE

View Article Online
View Journal | View Issue



Cite this: *Chem. Commun.*, 2025, **61**, 13807

# A repertoire of gold-based nanostructures with integrated optical and catalytic tunabilities

Hui Wang

Au nanoparticles exhibit geometry-dependent optical characteristics dictated by localized plasmon resonances and intriguing catalytic properties intimately tied to their atomic-level surface structures. While the dimensions of well-performing plasmon resonators typically range from tens of nanometers to submicrons, heterogeneous catalysis usually entails the use of much smaller nanoparticulate Au catalysts in the sub-5 nm size regime. Due to such a size gap, merging optical and catalytic tunabilities in a single Au nanoparticle has been a challenging task. In this feature article, I review several paradigm-shifting strategies for integrating tunable optical and catalytic properties within single Au-based nanostructures that are experimentally realizable. These strategies include nanoscale surface roughening of Au nanoparticles, creation of nanoporosity inside Au nanoparticles, facet control of anisotropic Au nanostructures, growth of Au nanocrystals with intrinsic structural chirality, and alloying Au with other metal elements in nanoparticles. By going through several case studies, I further elaborate on how the optical and catalytic properties can be judiciously tuned in a selection of dual-functional Au-based nanostructures to enable real-time monitoring of molecular transformations at the catalyst–adsorbate interfaces through *in situ* plasmon-enhanced spectroscopic measurements and kinetic modulation of catalytic/photocatalytic reactions through optical excitations of plasmonic electron oscillations and interband electronic transitions.

Received 16th July 2025,
Accepted 13th August 2025

DOI: 10.1039/d5cc04002g

rsc.li/chemcomm



*Department of Chemistry and Biochemistry, University of South Carolina, Columbia, South Carolina 29208, USA. E-mail: wang344@mailbox.sc.edu*

**Hui Wang**

*Hui Wang is currently a Full Professor in Department of Chemistry and Biochemistry at the University of South Carolina. He received his BS degree in Chemistry with honors from Nanjing University in 2001 (advisor: Jun-Jie Zhu) and his PhD degree in Physical Chemistry from Rice University in 2007 (advisor: Naomi Halas). He conducted postdoctoral research under the tutelage of Paul Barbara at the University of Texas at Austin. He joined the faculty of the University of South Carolina as a tenure-track Assistant Professor in 2010 and was promoted to an Associate Professor with tenure in 2016. His current research focuses on nanoplasmonics and nanocatalysis.*

## 1. Introduction

Metallic nanoparticles exhibit intriguing optical properties dictated by nanoconfined collective oscillations of free electrons, known as localized plasmons.[1–9] Optical excitations of localized plasmons result in significantly amplified optical cross-sections at the resonant frequencies and locally enhanced electric fields near the nanoparticle surfaces.[1–9] Besides radiative decay through light scattering, the resonantly excited plasmons can also decay non-radiatively through Landau damping to produce nonthermal hot carriers across the Fermi level within the conduction band of the metals.[10–13] These energetic hot carriers, far from the thermal equilibrium, can either be extracted and harnessed for photocatalysis or undergo multistep carrier relaxation and thermalization processes to generate heat within the metal lattices, an effect known as photothermal transduction.[10–13] In principle, nanoparticles made of any metal element in the periodic table can sustain localized plasmons as long as they contain a certain concentration of free electrons. However, the plasmonic behaviors of metallic nanoparticles are intrinsically tied to the material compositions, varying drastically from metal to metal.[14] From a materials design perspective, well-performing plasmon resonators should not only have high quality factors (defined as the resonance frequency-to-bandwidth ratios) but also be chemically stable and easily processable. Therefore, coinage metals,

especially Au and Ag, have long been considered as ideal candidates for constructing plasmonic materials and devices.[14,15] Although nanoparticles made of some non-coinage metals, such as Al[16,17] and Mg,[18] may also function as well-behaving plasmon resonators within certain spectral ranges, it remains challenging to leverage their plasmonic properties for practical applications due to highly reactive chemical nature of these metal elements and the difficulties in synthesizing and preserving these nanostructures. Nanoparticles made of semiconductors, such as metal chalcogenides,[19–27] oxides,[28–35] nitrides,[36,37] and phosphides,[38,39] may also exhibit metal-like plasmonic behaviors when they are doped with cation/anion vacancies or other ionized species to achieve appropriate free carrier concentrations. However, the plasmon resonance frequencies and quality factors of these doped semiconductor nanoparticles are typically far lower than those of Au and Ag nanoparticles. While Ag has the highest quality factor among all metals with minimal plasmon damping,[14] Au nanostructures appear more appealing than their counterparts made of Ag for plasmon-related applications in many cases benefiting from their greater chemical stability, biocompatibility, and versatility in surface functionalization. The dimensions, shapes, and interior structures of Au nanoparticles can all be precisely tailored through deliberately designed colloidal syntheses, which enables us to fine-tune the plasmon-dominated optical properties for targeted applications.[40–45]

Besides their fascinating optical properties, Au nanoparticles have also been of tremendous interest to the heterogeneous catalysis community. Although bulk Au appears catalytically inert, nanoparticulate Au in the sub-5 nm size regime can efficiently catalyze a series of important chemical reactions under mild and environmentally friendly conditions with enhanced chemoselectivity not readily attainable by other noble metal nanocatalysts.[46–54] Sub-5 nm Au nanoparticles dispersed on oxide- or carbon-based support materials exhibit intriguing size- and support-dependent catalytic behaviors.[48,50,55–60] Since the initial discovery of low-temperature CO-oxidation catalyzed by oxide-supported Au nanoparticles in 1980s,[61] Au-based heterogeneous nanocatalysis has been a highly active research area fully of fundamentally interesting open questions and exciting opportunities for transformative technological innovations.

The past decade has witnessed ever-increasing research interests in merging plasmonic and catalytic tunabilities within one unified nanomaterial platform. In the case of Au nanostructures, however, plasmonics and catalysis call for materials dimensions on two strikingly different, non-overlapping length-scales. Strong plasmon resonances with tunable resonant frequencies, well-defined spectral lineshapes, and large local-field enhancements become attainable when tailoring the particle dimensions in the subwavelength size regime ranging from tens of nanometers to submicrons, whereas the Au nanoparticles utilized for heterogeneous catalysis are typically smaller than 5 nm. In the sub-5 nm particle size regime, the behaviors of free electrons start to deviate from the classical plasmonic model due to modifications of the electronic band structures of Au,[62,63] resulting in strongly dampened resonances and diminished local-field enhancements. Bridging such a critical size gap to implement desired plasmonic and catalytic properties within a single Au nanoparticle has been a challenging task. This feature article elaborates on strategies for integrating optical and catalytic tunabilities in several deliberately designed and experimentally realizable Au-based nanostructures. The plasmonic-catalytic dual-functionalities contrived in these nanostructures not only enable use of plasmon-enhanced spectroscopies, such as surface-enhanced Raman scattering (SERS),[64–66] as *in situ* molecular fingerprinting tools for detailed mechanistic studies of catalytic reactions but also create unique opportunities for leveraging plasmonic effects to either energetically drive or kinetically boost molecular transformations on nanocatalyst surfaces.

## 2. Strategies for tuning the plasmonic properties of Au nanostructures

A solid sphere is the geometrically simplest, isotropic shape a nanoparticle can adopt. Within the quasi-static limit where the particle size is substantially smaller than the wavelength of the incident light, only the dipolar oscillations of free electrons contribute to the extinction of light, which is the sum of absorption and scattering,[67] at the plasmon resonance frequencies. The scattering-to-absorption ratio increases with the particle size.[67] In the size window of 5–100 nm, spherical Au nanoparticles exhibit a single light extinction peak signifying the dipolar plasmon resonances in the green portion of the visible spectrum.[68–70] In larger Au nanospheres beyond the quasi-static limit, the extinction spectral features of higher-order multipolar plasmon modes, such as quadrupole and octupole resonances, become prominent, while the dipole plasmon band is redshifted and significantly broadened due to the phase retardation effect.[68–70] Colloidal Au nanoparticles exhibiting spherical or quasi-spherical shapes have been synthesized in a size-controlled manner both within and beyond the quasi-static limit, and the experimentally observed size-dependency of their plasmonic features is in excellent agreement with theoretical predictions.[68–70]

Although spherical Au nanoparticles exhibit rather limited plasmonic tunability, breaking the particle symmetry or introducing hollow interior structures, as schematically illustrated in Fig. 1(A), may drastically enhance the plasmonic tunability of Au nanoparticles. Symmetry-breaking of Au nanoparticles can be accomplished through seed-mediated anisotropic nanocrystal growth processes. Au nanorods, derived from asymmetric growth of single-crystalline or pentatwinned Au seeds, represent a prototypical quasi-one-dimensional nanostructure with reduced symmetry and tunable plasmonic properties.[71–78] Experimentally synthesized Au nanorods typically exhibit a quasi-cylindrical morphology (Fig. 1(B)) with precisely tunable particle volumes and aspect ratios (length-to-width ratios). An Au nanorod responds to the polarization of incident light in an anisotropic manner, resulting in a transverse plasmon band in the wavelength range similar to that of nanosphere plasmons and a longitudinal plasmon band, which shifts to longer

 

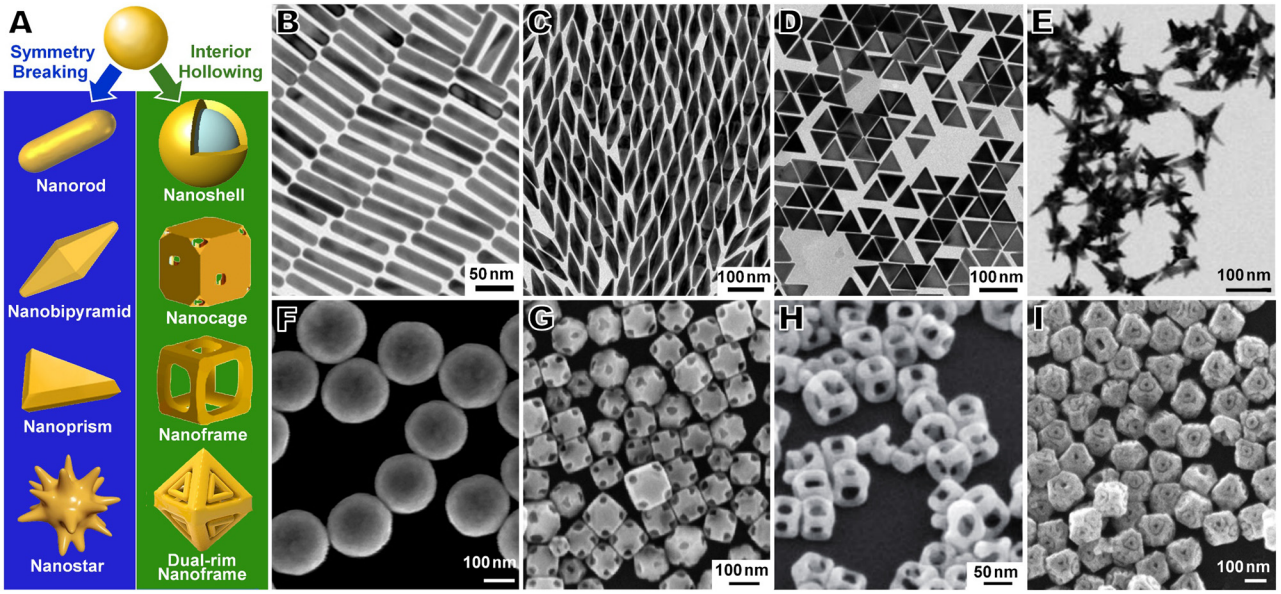


Fig. 1 (A) Various anisotropic and hollow Au nanostructures exhibiting tunable plasmonic properties. Transmission electron microscopy (TEM) images of (B) single-crystalline nanorods, (C) nanobipyramids, (D) nanoprisms, and (E) nanostars. Scanning electron microscopy (SEM) images of (F) nanoshells ($SiO_2$ core and Au shell), (G) nanocages, (H) nanoframes, and (I) dual-rim nanoframes. Adapted with permission from (B) ref. 72 (Copyright 2013 American Chemical Society), (C) ref. 81 (Copyright 2017 American Chemical Society), (D) ref. 84 (Copyright 2014 American Chemical Society), (E) ref. 89 (Copyright 2022 American Chemical Society), (F) ref. 99 (Copyright 2007 American Chemical Society), (G) ref. 109 (Copyright 2006 American Chemical Society), (H) ref. 110 (Copyright 2008 Springer Nature), and (I) ref. 111 (Copyright 2022 Springer Nature).

wavelengths as the particle aspect ratio progressively increases.[79] The local-field enhancements at the ends of Au nanorods are also aspect ratio-dependent and can be substantially higher than those achievable on spherical Au nanoparticles.[79] Au nanobipyramids are considered as structurally analogous to Au nanorods.[80–82] Experimentally synthesized Au nanobipyramids, each of which has a 5-fold rotational symmetry with two sharp tips (Fig. 1(C)), are derived from anisotropic growth of pentatwinned Au seeds. The plasmonic characteristics of Au nanobipyramids are determined by not only the particle aspect ratios but also the sharpness of the tips.[83] In comparison to Au nanorods, Au nanobipyramids exhibit narrower plasmon bandwidths and higher local-field enhancements.[83] Unlike their single-crystalline and pentatwinned counterparts, singly twinned Au nanocrystals may evolve into quasi-two-dimensional nanostructures, such as Au nanoprisms (Fig. 1(D)), through seed-mediated anisotropic growth.[84,85] Due to its intrinsic structural anisotropy, an Au nanoprism supports various in-plane and out-of-plane plasmons at distinct resonant frequencies.[86–88] In an Au nanoprism, the lateral dimensions, the thickness, and the tip sharpness all become critical geometric parameters determining the resonant frequencies, spectral lineshapes, and local-field enhancements of various plasmon modes.[84–88] Structural anisotropy may also be developed in multi-twinned Au nanocrystals to form multi-branched nanoparticles, known as nanostars (Fig. 1(E)).[89–96] The plasmonic characteristics of an Au nanostar are determined by the aspect ratios, tip sharpness, and relative orientations of the branched arms.[92–97] In an Au nanostar, the core serves as a nanoscale antenna that amplifies both the excitation cross-sections and the local fields in the hot spots near the tips.[97]

An alternative strategy for enhancing the plasmonic tunability involves the introduction of interior cavities to Au nanoparticles. One striking example is Au nanoshells, which are chemically synthesized by growing a thin shell of Au surrounding a spherical dielectric nanoparticle (Fig. 1(F)).[98,99] The plasmon resonance frequency of an Au nanoshell can be fine-tuned over a broad spectral range by tailoring its core size and shell thickness, and such plasmonic tunability in Au nanoshells essentially arises from the plasmon hybridization between a nanosphere and a cavity.[99,100] More complicated nanostructures derived from Au nanoshells, such as nanoeggs (nonconcentric nanoshells),[101] nanorice (ellipsoidal nanoshells),[102] and nanomatryoshkas (concentrically multilayered nanoshells),[100] exhibit more sophisticated plasmonic features with further enhanced tunability, and their detailed structure–property relationships can all be interpreted in the context of the plasmon hybridization model.[99,100] Au nanoparticles with hollow interior structures can also be synthesized through galvanic exchange reactions, in which a less-noble metal in a sacrificial nanoscale template undergoes oxidative etching while a more-noble metal is reduced and deposited onto the surfaces of the structurally evolving templates.[103] The primary driving force for particle hollowing during galvanic exchange is the Kirkendall effect, which is rooted in non-equivalent atomic interdiffusion rates of different metal elements.[104–107] Through deliberately controlled galvanic exchange, a series of hollow nanostructures made of Au-rich alloys with geometrically tunable plasmonic properties, such as nanocages (Fig. 1(G)) and nanoframes (Fig. 1(H)), can be selectively synthesized using single-crystalline Ag nanocubes as the templates.[108–110] Structurally and compositionally more complicated metallic hollow

nanostructures, such as dual-rim Au nanoframes (Fig. 1(I)), can be synthesized either through multistep regioselective deposition and etching or by coupling galvanic exchange with redox manipulation.[111–116] Increasing the interior architectural complexity of hollow nanoparticles not only further expands the plasmon tuning range but also creates intraparticle plasmonic hot spots with intense local fields exploitable for plasmon-enhanced spectroscopies.[117]

In addition to tailoring the sizes and geometries of Au nanoparticles, the plasmonic properties can be further tuned by changing the particle compositions or the local environments surrounding the Au nanoparticles. For example, incorporating other materials into Au-based nanostructures to form alloys, intermetallics, or heteronanostructures (core–shell, yolk–shell, and janus nanoparticles) may profoundly modify the optical properties of the nanoparticles.[14,118,119] With great success achieved in geometry- and composition-controlled colloidal synthesis and quantitatively understanding structure–property relationships, a solid knowledge foundation has started to emerge, built upon which the plasmonic properties of Au-based nanostructures can be precisely tuned and rationally optimized for widespread applications ranging from optical imaging and molecular sensing to biomedicine and photocatalysis.

## 3. Strategies for tuning the catalytic properties of Au nanostructures

The materials design principles for Au-based heterogeneous nanocatalysis are fundamentally different from those used for nanoplasmonics. In heterogeneous catalysis, the surface atoms in the outermost atomic layer of a catalyst material are the key players, while the bulk atoms in the materials' interior are not directly involved in the catalytic reactions. Therefore, the catalytic properties can be tuned most effectively by tailoring the atomic-level surface structures rather than the geometric shapes of Au nanoparticles. In crystalline Au materials forming face-centered cubic (fcc) lattices, bulk atoms have a coordination number (CN) of 12, while the atoms exposed on the materials surfaces are coordinatively unsaturated with lower CNs ranging from 6 to 9.[48,50] In the case of an Au nanoparticle adopting the classical Wulff structure, the surface atoms at the particle corners and edges have CNs of 6 and 7, respectively, while the CN of a surface atom at a terrace site is either 8 for a {100} facet or 9 for a {111} facet. When the particle size is below 2 nm, the particle surface is dominated by the corner and edge atoms. As the particle size increases, the fractions of both corner and edge atoms decrease and the particle surfaces become dominated by terraces when the particle size exceeds 5 nm (Fig. 2(A)).[50] Although Au nanoparticles larger than 5 nm appear catalytically inert, Au nanoparticles in the sub-5 nm size regime become highly active in catalyzing CO oxidation at low temperatures and their mass-specific catalytic activity increases drastically upon decrease of the particle size, an interesting phenomenon consistently observed in a variety of oxide support materials (Fig. 2(B)).[50] These results strongly indicate that the Au surface atoms located at the particle corners and edges rather than those residing on the terraces serve as the primary active sites for catalytic CO oxidation benefiting from their lower CNs. However, such intriguing size-dependent activities observed in supported Au nanocatalysts should not be interpreted solely in the context of surface atomic coordination. First, in the sub-5 nm size regime, the electronic band energies of Au are shifted due to quantum size effects, which modifies the interactions between the Au catalysts and the reactant/intermediate/product molecules.[55,120] Second, the intrinsic catalytic activities of sub-5 nm Au nanoparticles can be significantly modified by the support materials due to strong metal–support interactions.[121–125] Third, Au nanocatalyst surfaces may undergo structural rearrangement under operando conditions (Fig. 2(C)),[126] causing the catalyst behaviors to change over time during the reactions. It remains challenging to fully delineate several intertwining effects on the catalytic behaviors of supported Au nanocatalysts.

Nanoporous Au, also known as Au nanosponges, has emerged as a unique class of free-standing metal catalysts ideal for detailed investigations of structure–property relationships without the complications caused by the support materials.[127,128] Nanoscale porosity can be introduced to bulk Au through percolation dealloying, which involves selective etching of the less-noble constituents in an alloy matrix and structural rearrangement of the nonleachable, more-noble components.[129] Au–Ag alloy membranes have been most widely utilized as the precursors for nanoporosity-evolving percolation dealloying, which leads to the formation of solid/void bicontinuous nanoporous Au membranes (Fig. 2(D)).[130,131] Although both the ligaments and pores exhibit feature sizes beyond 5 nm, the dealloyed nanoporous Au may even outperform oxide-supported sub-5 nm Au nanocatalysts in catalyzing certain reactions.[127,128,132–134] The remarkable catalytic activities of dealloyed nanoporous Au are intimately tied to the high abundance of undercoordinated atoms located at the kink sites and step edges on the locally curved ligament surfaces.[135] It is noteworthy that the dealloyed nanoporous catalysts are not made purely of Au, because it is impossible to completely remove the less-noble elements through percolation dealloying. The residual Ag atoms on the surfaces of dealloyed nanoporous Au may profoundly influence not only the catalytic activity but also the reaction selectivity in the case of catalytic oxidation reactions.[131,136] When exposing fully dealloyed nanoporous Au (<1 atomic% residual Ag) to an oxygen-deficient atmosphere composed of 1 volume% of $O_2$ and 2 volume% methanol, methanol is selectively converted to a partially oxidized product, methyl formate, without forming the fully oxidized product, $CO_2$, over a broad temperature range from 20 to 80 °C (Fig. 2(E)).[131] Increasing the residual Ag content to 2.5 atomic% leads to loss of selectivity for methyl formate, especially at reaction temperatures higher than 65 °C (Fig. 2(F)).[131] When the fraction of residual Ag is above 10 atomic%, $CO_2$ becomes the dominate product with negligible yields of methyl formate.[131]

Another class of Au nanostructures possessing high abundance of low-coordination surface atoms are nanocrystals

 

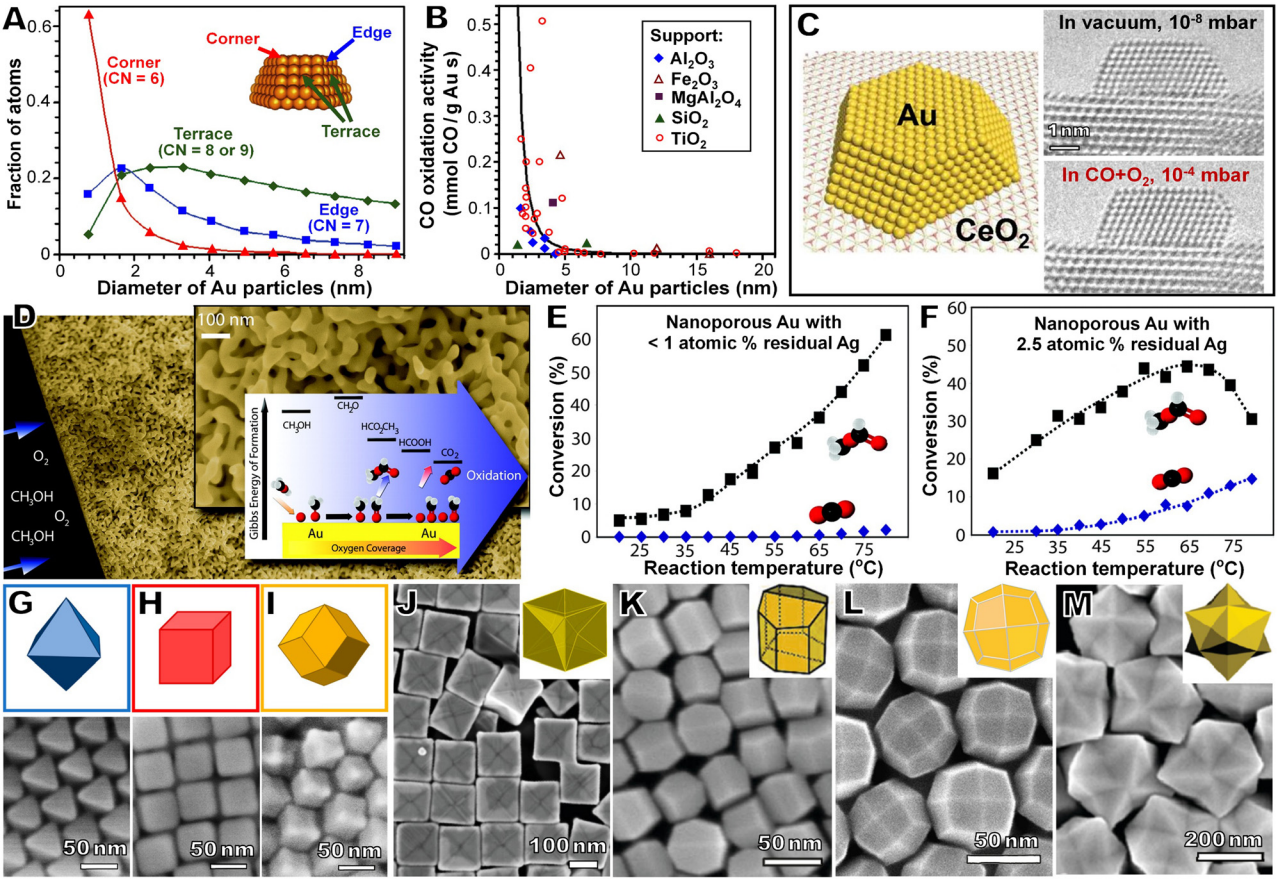


Fig. 2 (A) Calculated fractions of Au atoms at corners (red triangles), edges (blue squares), and terraces (green rhombuses) in uniform nanoparticles consisting of the top half of a truncated octahedron as a function of Au particle diameter. (B) Reported Au mass-specific catalytic activities for CO oxidation at 273 K as a function of Au particle diameter for different support materials. The solid curve shows the calculated particle size-dependent fractions of corner atoms on the surface of the top half of a truncated octahedral particle. (C) Cartoon illustration of a $CeO_2$-supported Au nanoparticle (left panel) and high-resolution TEM images highlighting the reconstruction of the {100} surface of a 4-nm Au nanoparticle with ~1000 atoms under operando conditions for CO oxidation (right panel). (D) SEM image of dealloyed nanoporous Au and schematic illustration of selective oxidation of methanol on Au surfaces. The catalytic activity and selectivity of the methanol oxidation over dealloyed nanoporous Au with (E) <1 atomic% of residual Ag (catalyst mass: 20.1 mg) and (F) 2.5 atomic% of residual Ag (catalyst mass: 20.6 mg). The total oxidation of methanol to $CO_2$ and partial oxidation of methanol to methyl formate are represented by blue rhombuses and black squares, respectively. The catalytic reactions were conducted under continuous flow conditions at different temperatures at a total gas stream of 50 standard cubic centimeters per minute. Cartoon illustrations (upper panels) and SEM images (lower panels) of (G) octahedral, (H) cubic, and (I) rhombic dodecahedral Au nanoparticles. SEM images of (J) Au concave nanocubes enclosed by {720} facets, (K) Au truncated ditetragonal nanoprisms enclosed by {310} facets, (L) trapezohedral Au nanocrystals enclosed by {310} facets, and (M) hexoctahedral Au nanocrystals enclosed by {321} facets. Adapted with permission from (A), (B) ref. 50 (Copyright 2007 Elsevier), (C) ref. 126 (Copyright 2018 National Academy of Sciences), (D)–(F) ref. 131 (Copyright 2010 American Association for the Advancement of Science), (G)–(I) ref. 141 (Copyright 2024 American Chemical Society), (J) ref. 142 (Copyright 2010 American Chemical Society), (K) ref. 143 (Copyright 2011 American Chemical Society), (L) ref. 144 (Copyright 2017 American Chemical Society), and (M) ref. 145 (Copyright 2012 American Chemical Society).

enclosed by high-index facets (at least one of the Miller indices greater than unity).[137,138] High-index facets are characterized by a high density of atomic steps and kinks, exhibiting increased catalytic activity in comparison to low-index facets.[139,140] For a single-crystalline fcc Au nanoparticle, there are three basic low-index faceting polyhedral geometries, an octahedron enclosed by 8 {111} facets (Fig. 2(G)), a cube enclosed by 6 {100} facets (Fig. 2(H)), and a rhombic dodecahedron enclosed by 12 {110} facets (Fig. 2(I)).[141] Through deliberate kinetic control and regioselective surface passivation during colloidal nanocrystal growth, surface convexity or concavity can be introduced to the basic low-index facets to produce Au nanocrystals that selectively adopt a series of exotic polyhedral shapes, each of which is exclusively enclosed by one specific type of high-index facets (see representative examples in Fig. 2(J)–(M)).[142–148] To form well-defined polyhedral shapes with fully developed crystallographic facets, experimentally synthesized high-index faceting Au nanocrystals are typically in the size range from tens of nanometers to submicrons. Although ideal for fundamental studies, these relatively large high-index faceting Au nanoparticles are of rather limited value for industrial applications because of their low surface-to-volume ratios.

# 4. Combining the best of both worlds: merging nanoplasmonics and nanocatalysis within the same Au-based nanostructures

In this section, I will elaborate on the strategies for merging plasmonic and catalytic tunabilities within single nanoscale entities by explicating the detailed structure–property relationships in a selection of rationally designed and experimentally realizable Au-based nanostructures. Taking full advantage of the integrated plasmonic-catalytic dual-functionalities, I will further discuss how to use plasmon-enhance spectroscopic tools for *in situ* monitoring of catalytic reactions and how to leverage various plasmonic effects to drive or boost chemical transformations on Au nanocatalyst surfaces.

## 4.1. Nanoscale surface roughening of Au nanoparticles

Introduction of nanoscale surface roughness to subwavelength Au nanoparticles provides a straightforward but effective pathway to drastically enhance both the plasmonic tunability and catalytic activity of the particles. Colloidal Au surface-roughened nanoparticles (SRNPs) can be synthesized through seed-mediated nanocrystal growth under kinetically controlled conditions, choosing sub-5 nm single-crystalline Au nanoparticles as the seeds, $HAuCl_4$ as the Au(III) precursor, cetyltrimethylammonium chloride (CTAC) as a surface-capping ligand, and ascorbic acid as a mild reducing agent, respectively.[149] As schematically illustrated in Fig. 3(A), the single-crystalline Au seeds may selectively evolve into several geometrically distinct Au nanostructures, depending on the rate of the nanocrystal growth, which can be tuned by adjusting either the concentration of ascorbic acid or the pH of the nanocrystal growth solution.[149] Fast nanocrystal growth favors full development of high-index facets, leading to the formation of single-crystalline trisoctahedral (TOH) Au nanoparticles, each of which is enclosed by 24 equivalent {221} facets (Fig. 3(B)).[150] In contrast, slow nanocrystal growth favors the formation of low-index facets and twinned crystal structures, producing thermodynamically favored quasi-spherical nanoparticles (QSNPs) enclosed by alternating {100} and {111} facets (Fig. 3(C)).[149] When the Au nanocrystals grow at medium rates, both intraparticle crystal-twining and nanoscale surface texturing occur during seed-mediated growth, resulting in Au SRNPs exhibiting a nanotextured surface morphology (Fig. 3(D)).[149] By varying the Au(III)-to-seed ratio, the overall particle sizes of Au SRNPs can be precisely tuned over a broad range from $\sim$50 nm up to $\sim$500 nm, while well-preserving the nanotextured surface features.

Colloidal Au SRNPs exhibit size-dependent plasmonic features, with their plasmon resonance band shifting to longer wavelengths as their particle sizes increase (Fig. 3(E)).[149] When functioning as SERS substrates, Au SRNPs also significantly outperform Au QSNPs because nanoscale surface roughening gives rise to substantially higher local-field enhancements on the particle surfaces (Fig. 3(F) and (G)). Under resonant excitations, the apparent enhancement factors of SERS signals on an individual Au SRNP can approach $\sim 10^7$, more than 3 orders of magnitude higher than those achievable on individual Au QSNPs.[149] The intense local-fields at the roughened Au nanoparticle surfaces provide sufficiently high sensitivity for SERS-based characterization of surface-adsorbed molecular ligands at monolayer and sub-monolayer coverages with minimal interference by the unbound ligands in the solution phase. Therefore, SERS can be utilized as a unique *in situ* spectroscopic tool to study dynamic interfacial behaviors of molecular ligands on locally curved Au surfaces without the need to separate the colloidal Au SRNPs from their native environments (see schematic illustration in Fig. 3(H)).[151] The local surface curvature of Au SRNPs varies significantly from site to site, providing both high-curvature and low-curvature sites on open surfaces directly accessible by molecular ligands. Organothiol ligand molecules exhibit intriguing chemisorption behaviors that are sensitive to the local surface curvature at the ligand-binding sites.[151] Comparative studies of ligand binding to Au SRNPs and QSNPs reveal that chemisorption of organothiols to high-curvature Au surfaces is kinetically faster but thermodynamically less favored in comparison to ligand binding to low-curvature surface sites (Fig. 3(I) and (J)).[151] While the binding of thiolated ligands to low-curvature Au surfaces is a non-cooperative process that can be fully described by the classical Langmuir adsorption model, ligand binding to high-curvature surface sites becomes cooperative with Hill coefficients around 2. The results of SERS-based ligand titration and kinetic measurements clearly show that the nanoparticle surface curvature plays crucial roles in regulating nanoparticle–adsorbate interactions.

Au SRNPs with plasmonic-catalytic dual-functionalities are ideal for SERS-based spectroscopic monitoring of catalytic reactions. Au SRNPs, which are rich in undercoordinated surface atoms at their locally curved surface sites, appear far more active than Au QSNPs with comparable particle sizes in catalyzing the reduction of *para*-nitrophenol by borohydride in an aqueous environment,[152] a model transfer hydrogenation reaction widely used for assessing the performances of metallic nanocatalysts. To gain further mechanistic insights, SERS has been utilized as an *in situ* molecule-fingerprinting tool to track the structural evolution of *para*-nitrothiophenol (pNTP) chemisorbed to colloidal SRNPs upon exposure to borohydride (Fig. 3(K)).[152] The *in situ* SERS results clearly reveal that pNTP is converted to *para*-aminothiophenol (pATP) on the locally curved Au surfaces in a chemoselective manner before pATP eventually desorbs from Au surfaces. A key intermediate produced during the reaction is identified to be *p*,*p*′-dimercaptoazobenzene (DMAB), which is derived from reductive bimolecular coupling of surface-adsorbed pNTP. The reaction mechanism proposed based on the temporal evolution of SERS spectra is schematically illustrated in Fig. 3(L). The *in situ* SERS measurements conducted on ligand-capped Au SRNPs during catalytic reactions provide detailed kinetic information and mechanistic insights that are not readily attainable through other measurements.[152]

The unique combination of tunable plasmonic and catalytic properties in Au SNRPs enables not only SERS-based mechanistic studies but also plasmon-mediated kinetic modulation of

 

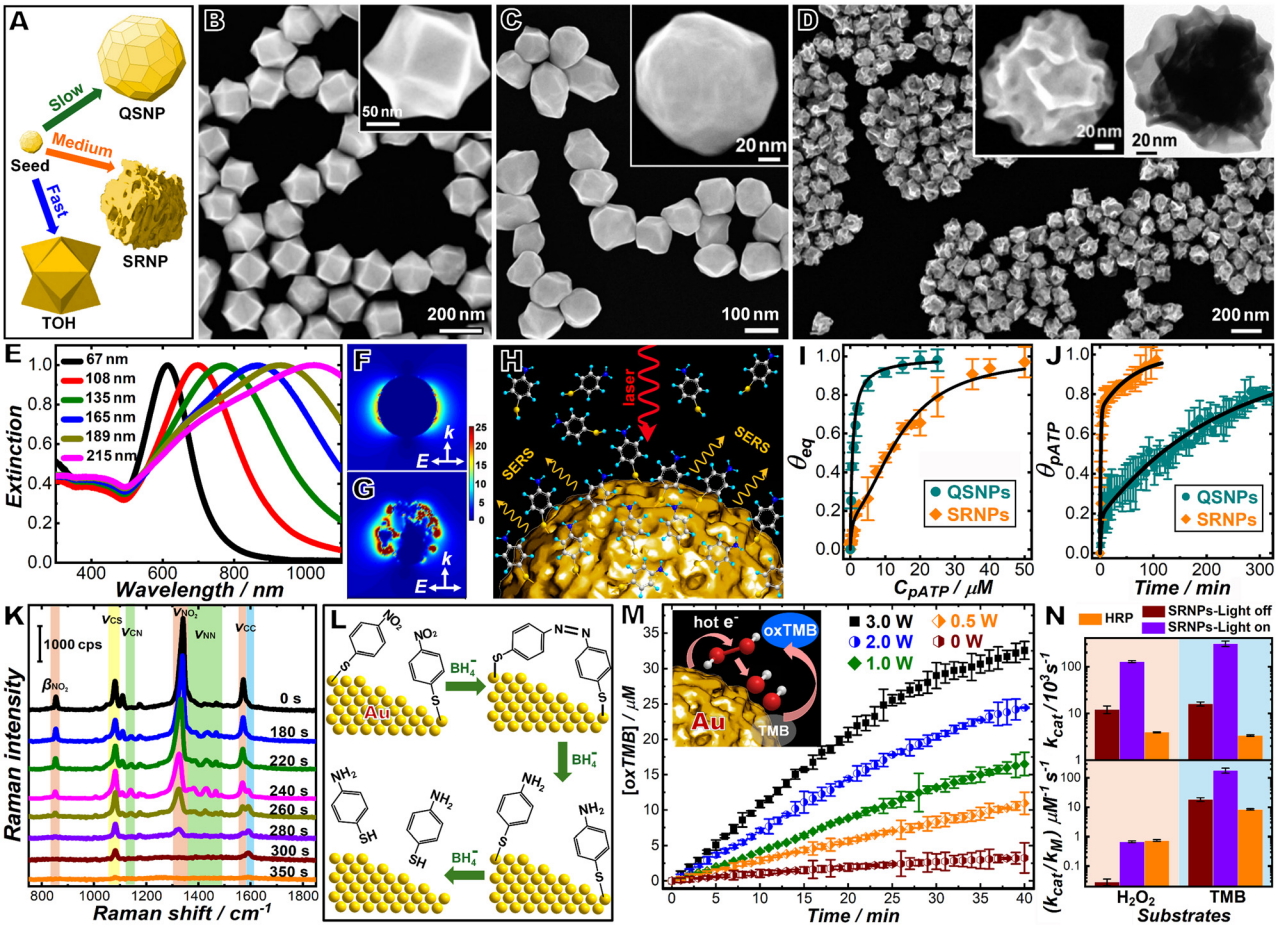


Fig. 3 (A) Schematic illustration of seed-mediated growth of Au TOH nanoparticles, QSNPs, and SRNPs. SEM images of Au (B) TOH nanoparticles, (C) QSNPs, and (D) SRNPs. Higher-magnification SEM images of individual nanoparticles are shown in the insets of panels B, C, and D, and the upper-right inset in panel D shows a TEM image of an individual Au SRNP. (E) Optical extinction spectra of colloidal Au SRNPs with various average particle diameters as labeled in the figure. Cross-sectional view of the local-field enhancements of an Au (F) QSNP and (G) SRNP with a diameter of 108 nm at 785 nm plane wave excitation calculated using the finite-difference time domain method. (H) Cartoon illustration of using SERS to study the interfacial adsorption/desorption behaviors of thiolated ligands on locally curved surfaces of an Au SRNP. (I) Adsorption isotherms (quantified based on the SERS peak intensity at 1078 $cm^{-1}$) of pATP on Au SRNPs and QSNPs. (J) Temporal evolution of apparent pATP coverage ($\theta_{pATP}$) upon exposure of colloidal Au SRNPs and QSNPs to 50 μM pATP. The solid black curves in panels I and J show the curve fitting results. (K) Temporally evolving SERS spectra collected from pNTP-coated Au SRNPs at different reaction times after exposure to 30 mM $NaBH_4$. (L) Schematic illustration of the reaction mechanism of transfer hydrogenation of pNTP adsorbates on the Au surface. (M) Temporal evolution of oxidized TMB (oxTMB) concentrations during the reactions catalyzed by Au SRNPs under illumination by a continuous wave 785 nm laser at various excitation powers. The inset illustrates the reaction mechanism of Au-catalyzed TMB oxidation in the presence of $H_2O_2$ under light illumination. (N) Turn-over numbers (upper panel) and catalytic efficiencies (lower panel) of HRP in the dark and Au SRNPs in the dark and under laser illumination (785 nm, 3.0 W). Adapted with permission from (B) ref. 150 (Copyright 2014 American Chemical Society), (C), (E), (F) and (G) ref. 149 (Copyright 2014 American Chemical Society), (D), (K) and (L) ref. 152 (Copyright 2014 American Chemical Society), (H)–(J) ref. 151 (Copyright 2017 American Chemical Society), and (M) and (N) ref. 155 (Copyright 2020 American Chemical Society).

catalytic reactions. A particularly interesting property of Au nanoparticles is that they can mimic natural enzymes, such as peroxidases, in terms of catalytic behaviors. Enzyme-mimicking inorganic nanomaterials, known as nanozymes, are structurally more robust than the natural enzymes, exhibiting enhanced catalytic durability over a broader range of working conditions.[153,154] However, the catalytic efficiencies of Au nanozymes are rather low in comparison to those of natural enzymes in numerous cases, and there is still plenty of room for further improvement. Colloidal Au SRNPs are unique plasmonically tunable nanozymes, allowing us to fine-tune their enzyme-mimicking activities through plasmonic excitations. Au SRNPs significantly outperform QSNPs when executing their peroxidase-mimicking functions both in dark and under light illumination.[155] In dark reactions, both natural peroxidases and Au nanozymes can effectively mediate the electron transfer from organic substrate molecules to $H_2O_2$, which catalyzes the homolytic split of surface-adsorbed $H_2O_2$ to generate hydroxyl radicals. The undercoordinated Au atoms at the locally curved surfaces serve as the primary active sites responsible for the remarkable peroxidase-mimicking activities of Au SRNPs.[155] Under plasmon excitations, the photoexcited hot electrons in Au SRNPs can be harnessed to kinetically maneuver the electron transfer from Au to surface-adsorbed $H_2O_2$ (see a

schematic illustration in the inset of Fig. 3(M)). The injection of a plasmonic hot electron into the antibonding orbital of a surface-adsorbed $H_2O_2$ triggers the homolytic cleavage of the O–O bond and gives rise to enhanced reaction kinetics. 3,3′,5,5′-Tetramethylbenzidine (TMB) has been a chromogenic substrate widely used for assessing the catalytic activities of both natural peroxidases and nanozymes. The kinetic features of Au-catalyzed TMB oxidation by $H_2O_2$ can be well-described by the Michaelis–Menton steady state kinetic model both in dark and under plasmonic excitations, with the initial velocity increasing linearly with the excitation power (Fig. 3(M)). The turn-over numbers ($k_{cat}$) and catalytic efficiencies ($k_{cat}/k_m$, where $k_m$ is the Michaelis constant) of Au SRNPs become substantially higher than those of horseradish peroxidase (HRP) upon resonant excitations of plasmons (Fig. 3(N)). Here, the $k_{cat}$ of Au SRNPs is essentially a descriptor of the overall nanozyme activities at the nanoparticulate level rather than at single active sites. While there is only one active site in each HRP molecule, each Au SRNP possesses a large number of active sites on its surface. It remains challenging, however, to quantify the exact number of active sites per particle, and the catalytic activity at individual active sites may vary drastically from location to location on the nanozyme surfaces.

### 4.2. Introduction of nanoporosity to Au nanoparticles

The plasmonic and catalytic properties of an Au nanoparticle can be drastically modified upon creation of nanoscale porosity. While porous Au nanoparticles can be synthesized through multistep procedures involving the use of either hard or soft templates,[156–159] percolation dealloying of Au-containing alloys provides a more straightforward strategy for creating nanoscale porosity with structural and compositional control at a higher level of precision and versatility.[160–162] The nanoporosity evolution during percolation dealloying entangles atomic dissolution, deposition, and migration both at the solid/electrolyte interfaces and in the bulk of alloy matrices, which can be well-described by a surface-diffusion continuum model proposed by Erlebacher and coworkers.[129] Taking Au–Ag bulk alloys as an example, chemical or electrochemical dealloying is initiated upon dissolution of Ag atoms exposed on the alloy surfaces, which produces undercoordinated Au surface atoms at the solid/electrolyte interface. These undercoordinated Au surface atoms undergo rapid surface migration to agglomerate into local patchy islands, while patches of undealloyed materials remain exposed to the etching environment. Continuous etching of Ag atoms and surface migration of Au atoms at the dealloying frontier creates a network of branched pore channels, which eventually evolves into a solid/void bicontinuous nanoporous structure through pore expansion and ligament coarsening.

Much of the knowledge gained from macroscopic bulk alloy materials also applies to nanoparticulate alloys, which provides the guiding principles for structural and compositional control of spongy metallic nanoparticles through percolation dealloying. Spongy Au–Ag alloy nanoparticles with tunable pore sizes, ligament thicknesses, and Ag : Au stoichiometric ratios can be synthesized through percolation dealloying of Au–Ag alloy nanoparticles (Fig. 4(A)).[163] Au@Ag core–shell nanoparticles may evolve into fully alloyed Au–Ag bimetallic nanoparticles upon thermal annealing at high temperatures above 900 °C. Prior to thermal annealing, each Au@Ag core–shell nanoparticle is coated with a $SiO_2$ shell to form a triple-layer nanostructure (denoted as Au@Ag@$SiO_2$), which effectively prevents the particles from sintering during thermal annealing. After the Ag and Au atoms are fully intermixed, the alloy@$SiO_2$ core–shell nanoparticles (denoted as AuAg alloy@$SiO_2$) are treated with an alkaline solution to selectively etch $SiO_2$, which converts the dense $SiO_2$ shell into an ultrathin (< 5 nm) porous shell. The alloy nanoparticles encased in ultrathin silica shells [denoted as AuAg alloy@$SiO_2$(thin)] undergo percolation dealloying when exposed to concentrated nitric acid. Besides the formation of nanoporosity, the overall particle sizes also shrink significantly during percolation dealloying, resulting in the formation of yolk@shell nanoparticles (denoted as pAuAg@void@$SiO_2$), each of which consists of a porous Au–Ag alloy yolk inside an ultrathin $SiO_2$ shell (Fig. 4(B)). Introduction of nanoporosity leads to a spectral redshift and line-shape broadening of the plasmon resonance band in the extinction spectra (Fig. 4(C)) due to the plasmon coupling between nanoligaments.[163] As an increasing amount of Ag is removed from the alloy nanoparticles, both the pore volumes and ligament thicknesses increase, resulting in a spectral blue-shift of the plasmon resonance bands. Benefiting from the high densities of intraparticle hot spots (inset of Fig. 4(C)) and large mass-specific open surface areas, the SERS signals of Raman reporters, such as crystal violet, on a single pAuAg@void@$SiO_2$ particle become orders of magnitude higher than those achievable on a single nonporous Au nanoparticle (Fig. 4(D)).[163]

Spongy nanoparticles can also be derived from Au–Cu alloy nanoparticles through percolation dealloying (Fig. 4(E)).[164] Au–Cu alloy nanoparticles can be synthesized by thermally reducing Au@$Cu_2O$ core–shell nanoparticles either in an $H_2$-containing atmosphere or in a polyol solvent at reaction temperatures (< 400 °C) much lower than that required for the Au–Ag alloying.[106,164] The particle sizes and Au : Cu stoichiometric ratios of the alloy nanoparticles are predetermined by the core and shell sizes of the parental Au@$Cu_2O$ core–shell nanoparticles. Besides the atomically disordered alloys, atomically ordered intermetallic phases, specifically $AuCu_3$-L12 and AuCu-L10, can also emerge in the bimetallic nanoparticles derived from Au@$Cu_2O$ core–shell nanoparticles.[106] While nanoparticles made of the intermetallic phases and Au-rich alloys (Cu : Au ratios < ~70%) undergo surface dealloying without forming intraparticle nanoporosity upon exposure to etchants, Cu-rich alloy nanoparticles with Cu : Au stoichiometric ratios higher than ~70% evolve into spongy nanoparticles through percolation dealloying (Fig. 4(F)).[164] The fully dealloyed spongy Au nanoparticles (< 3 atomic% residual Cu) can be utilized as nanoscale carriers to assemble multi-functional drug vehicles for the synergistic chemo-photothermal therapy (Fig. 4(G)).[165] Doxorubicin (DOX), a widely used chemotherapeutic anticancer drug, can be loaded into the dealloyed spongy Au nanoparticles at controlled loading dosages through electrostatic interactions. A pH- and thermo-dual stimuli responsive copolymer–liposome

 

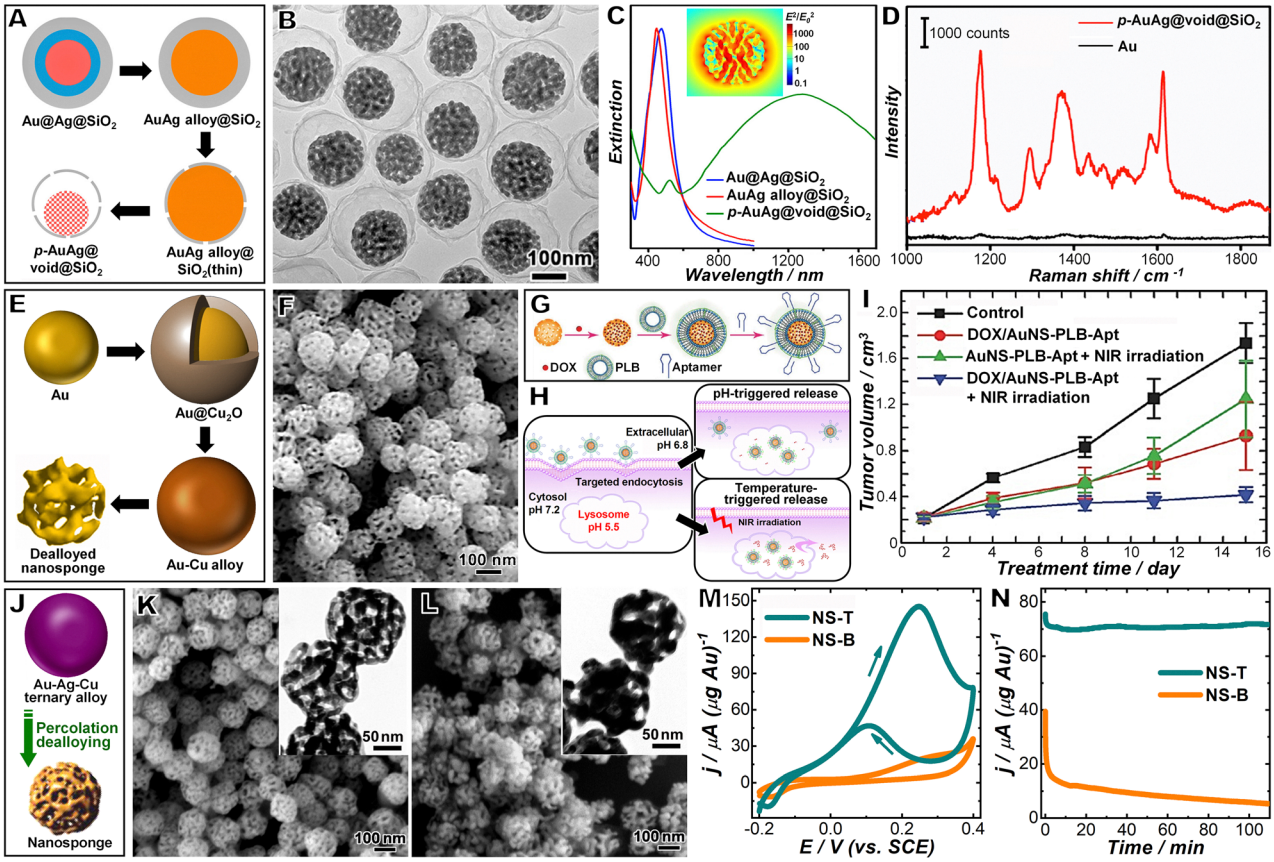


Fig. 4 (A) Scheme illustrating synthesis of *p*-AuAg@void@$SiO_2$ yolk–shell nanoparticles through percolation dealloying. (B) TEM image of *p*-AuAg@void@$SiO_2$ nanoparticles. (C) Optical extinction spectra of colloidal Au@Ag@$SiO_2$, AuAg alloy@$SiO_2$, and *p*-AuAg@void@$SiO_2$ nanoparticles. (D) SERS spectra of crystal violet on the surfaces of an individual non-porous Au nanoparticle and a *p*-AuAg@void@$SiO_2$ nanoparticle. (E) Synthesis of Au–Cu bimetallic nanosponges through stepwise alloying and dealloying processes. (F) SEM image of spongy $Au_{0.72}Cu_{0.28}$ alloy nanoparticles synthesized through percolation dealloying of $Au_{0.19}Cu_{0.81}$ alloy nanoparticles in 0.5 M $HNO_3$ for 3 h. Schematic illustration of (G) construction of Au nanosponge (AuNS)-based drug vehicles and (H) working mechanism of pH- and temperature-triggered drug release from the AuNS-based drug vehicles. (I) Change of tumor volume after mice were intravenously injected with phosphate-buffered saline (control), AuNS-PLB-Apt nanoconstructs with NIR irradiation, DOX@AuNS-PLB-Apt nanoconstructs, and DOX@AuNS-PLB-Apt nanoconstructs with NIR irradiation. (J) Percolation dealloying of Au–Ag–Cu ternary alloy nanoparticles. SEM and TEM (insets) images of (K) NS-T nanoparticles derived from percolation dealloying of Au–Ag–Cu ternary alloy nanoparticles and (L) NS-B nanoparticles derived from percolation dealloying of Au–Cu binary alloy nanoparticles. (M) Cyclic voltammetry and (N) chronoamperometry curves of NS-T and NS-B in 0.5 M KOH electrolyte solutions containing 1 M methanol. Adapted with permission from (A)–(D) ref. 163 (Copyright 2016 American Chemical Society), (E) and (F) ref. 164 (Copyright 2016 American Chemical Society), (G)–(I) ref. 165 (Copyright 2016 John Wiley and Sons), and (J)–(N) ref. 166 (Copyright 2016 American Chemical Society).

bilayer (PLB) is conjugated to the surfaces of DOX-loaded spongy Au nanoparticles to generate a smart gate-keeping layer for precise control of the drug release profiles. The surfaces of the copolymer–liposome-coated spongy nanoparticles are further functionalized with an RNA aptamer that not only specifically targets the Epithelial Cell Adhesion Molecule overexpressed on the tumor cell surfaces but also enhances the cell internalization of the nanoconstructs. The colloidal spongy nanoparticles also exhibit broadband plasmon resonances in the near-infrared (NIR) water window, which can be harnessed for local tumor hyperthermia and photothermally triggered drug release. The as-constructed drug vehicles enable simultaneous delivery of DOX and heat to targeted cells (Fig. 4(H)). Employing the MCF-7 tumor-bearing nude mice as a model system, *in vivo* studies reveal that synergized chemo-photothermal therapy using Au nanosponge-based drug vehicles offers remarkable therapeutic efficacy with minimized side effects (Fig. 4(I)).

The dealloyed metallic spongy nanoparticles have large mass-specific surface areas, high densities of active surface sites, and great electron conductivity in their nanoporous frames, all of which are highly desired for electrocatalysis.[164] Au–Cu bimetallic spongy nanoparticles derived from percolation dealloying of Au–Cu alloy nanoparticles exhibit tunable catalytic activities toward electrochemical oxidation of liquid alcohols, such as methanol, ethanol, iso-propanol, and ethylene glycol.[164,166] During percolation dealloying, the leaching of Cu atoms from the alloy matrices creates atomically under-coordinated surface sites that are catalytically active for alcohol electro-oxidation, whereas the coarsening of nanoligaments causes both the mass-specific surface area and the surface-

density of active sites to decrease. The optimization of electrocatalytic activities of dealloyed spongy nanoparticles essentially relies on the precise control of the ligament thickness and surface-density of undercoordinated atoms, which can be achieved by regulating the relative rates of Cu leaching with respective to ligament coarsening during percolation dealloying.

Both the activity and durability of the dealloyed Au nanocatalyts can be significantly further enhanced upon incorporation of residual Ag, which can be achieved through percolation dealloying of Au–Ag–Cu trimetallic alloy nanoparticles (Fig. 4(J)).[166] As shown in Fig. 4(K) and (L), the fully dealloyed nanosponge particles obtained from dealloying of Au–Ag–Cu ternary alloy nanoparticles (denoted as NS-T) exhibit substantially thinner ligaments, smaller pore sizes, and higher densities of surface active sites in comparison to their Ag-free counterparts derived from Au–Cu binary alloy nanoparticles (denoted as NS-B) as the consequence of accelerated Cu leaching and hindered ligament coarsening. The dealloyed NS-T particles exhibit remarkably higher electrocatalytic activities than the Ag-free NS-B particles (Fig. 4(M)). The residual Ag in the dealloyed NS-T particles keeps the catalytically active surface atoms from structural reconstruction during electrocatalytic reactions, giving rise to enhanced catalytic durability (Fig. 4(N)). Structurally and compositionally more complicated spongy nanoparticles can be synthesized when further coupling the percolation dealloying with galvanic exchange. For example, when reacting Au–Cu alloy nanoparticles with $H_2PtCl_6$ in ethylene glycol at 140 °C, an ultrathin Au–Pt alloy skin ($\sim$1 nm thick) forms on the nanoligament surfaces as the consequence of dynamic interplay between Cu–Pt galvanic exchange and percolation dealloying of Au–Cu alloys.[167] In comparison to their Pt-less counterparts, the Au–Pt alloy skin-covered spongy nanoparticles exhibit further enhanced electrocatalytic activities and durabilities for a variety of important reactions, such as formic acid oxidation and hydrogen evolution reactions.[167] These results, once again, highlight the importance of the synergisms among multiple metal elements present on the nanoligament surfaces in regulating the catalytic activity and durability of Au-based spongy nanocatalysts.

### 4.3. Facet control of anisotropic Au nanoparticles

In an anisotropic Au nanostructure, its catalytic properties can be tuned by tailoring the atomic-level surface structures, while preserving the plasmonic tunability associated with its structural anisotropy. A striking example is Au nanorods, which exhibit aspect ratio-dependent plasmonic properties and intrinsic catalytic activities intimately tied to the atomic coordinations on their locally curved surfaces. Although single-crystalline Au nanorods synthesized through seed-mediated growth are generally described as cylindrical particles capped by hemispherical ends, they are essentially enclosed by a variety of high-index and low-index crystallographic facets that are capped with surfactant molecules and Ag adatoms.[168] The detailed assignments of the Miller indices of local facets exposed on nanorod surfaces have long been controversial.[169–174] The catalytic activities vary drastically from site to site on the surfaces of individual Au nanorods,[175] and the detailed structure–property relationships remain challenging to elucidate due primarily to the presence of structural defects and ill-defined facets.

Developing well-defined crystallographic facets on single-crystalline Au nanorod surfaces creates unique dual-functional materials serving as both heterogeneous nanocatalysts and SERS substrates, enabling us to quantitatively compare the intrinsic catalytic activities of various types of Au facets through *in situ* SERS measurements. Precise control of nanorod facets can be achieved through kinetically controlled overgrowth of cylindrical Au nanorods co-guided by surface-capping molecular ligands and foreign ion additives. For example, cylindrical single-crystalline Au nanorods evolve into Au nanocuboids (NCB), each of which is enclosed by 6 {100} facets, through overgrowth in the presence of $Cu^{2+}$ ions and CTAC.[176] When switching from the CTAC monosurfactant to binary surfactant systems, surface convexity and concavity start to develop on the nanorod surfaces, resulting in the formation of high-index faceting convex nanocuboids (CVNCB) and concave nanocuboids (CCNCB) in benzyldimethylhexadecylammonium chloride (BDAC)/CTAC and cetyltrimethylammonium bromide (CTAB)/CTAC binary surfactant systems, respectively.[176] The aspect ratios of the Au NCBs, CVNCBs, and CCNCBs can all be precisely tuned by varying the aspect ratio of the Au nanorod seeds or by adjusting the $HAuCl_4$-to-seed ratio in the overgrowth solution, which allows us to tune the longitudinal plasmon resonance frequencies with respect to that of the excitation lasers to maximize the SERS enhancements. *In situ* SERS results reveal that the high-index faceting CVBCBs and CCNCBs are far more active in catalyzing the transfer hydrogenation of chemisorbed pNTP than the low-index faceting NCBs.[176]

The CVNCBs, also known as elongated tetrahexahedral (ETHH) nanoparticles, represent a single-crystalline nanorod-derived geometry enclosed exclusively by {*hk0*} high-index facets. Overgrowth of ETHH Au nanoparticles leads to selective formation of a series of anisotropic nanoparticle geometries enclosed by well-defined crystallographic facets, such as elongated trisoctahedral (ETOH), concave cuboidal (CCB), quasi-cuboidal (QCB), and elongated octahedral (EOH) nanoparticles.[177] Precise facet control of Au nanorods relies on the use of $Cu^{2+}$ ions and CTAB as a pair of surface-capping competitors to guide the facet evolution during nanorod overgrowth. As shown in Fig. 5(A)–(E), the Miller indices of the characteristic facets at the ends of the ETHH, ETOH, CCB, QCB, and EOH nanoparticles are {730}, {221}, {511}, {100}, and {111}, respectively. pNTP molecules chemisorbed on the Au nanoparticle surfaces are converted to pATP in a chemoselective manner upon exposure to ammonia borane, which severs as the hydrogen donor for the catalytic transfer hydrogenation reactions (Fig. 5(F)). The results of *in situ* SERS measurements (Fig. 5(G) and (H)) reveal that pNTP undergoes bimolecular coupling to form DMAB, followed by further reduction of DMAB to produce pATP. The pNTP-to-DMAB conversion is found to be kinetically slower than the DMAB-to-pATP conversion, serving as the rate-limiting step for the transfer hydrogenation reactions. Under NIR laser excitations, the SERS signals collected from colloidal samples are dominated by the molecular adsorbates residing in the longitudinal hot spots,

 

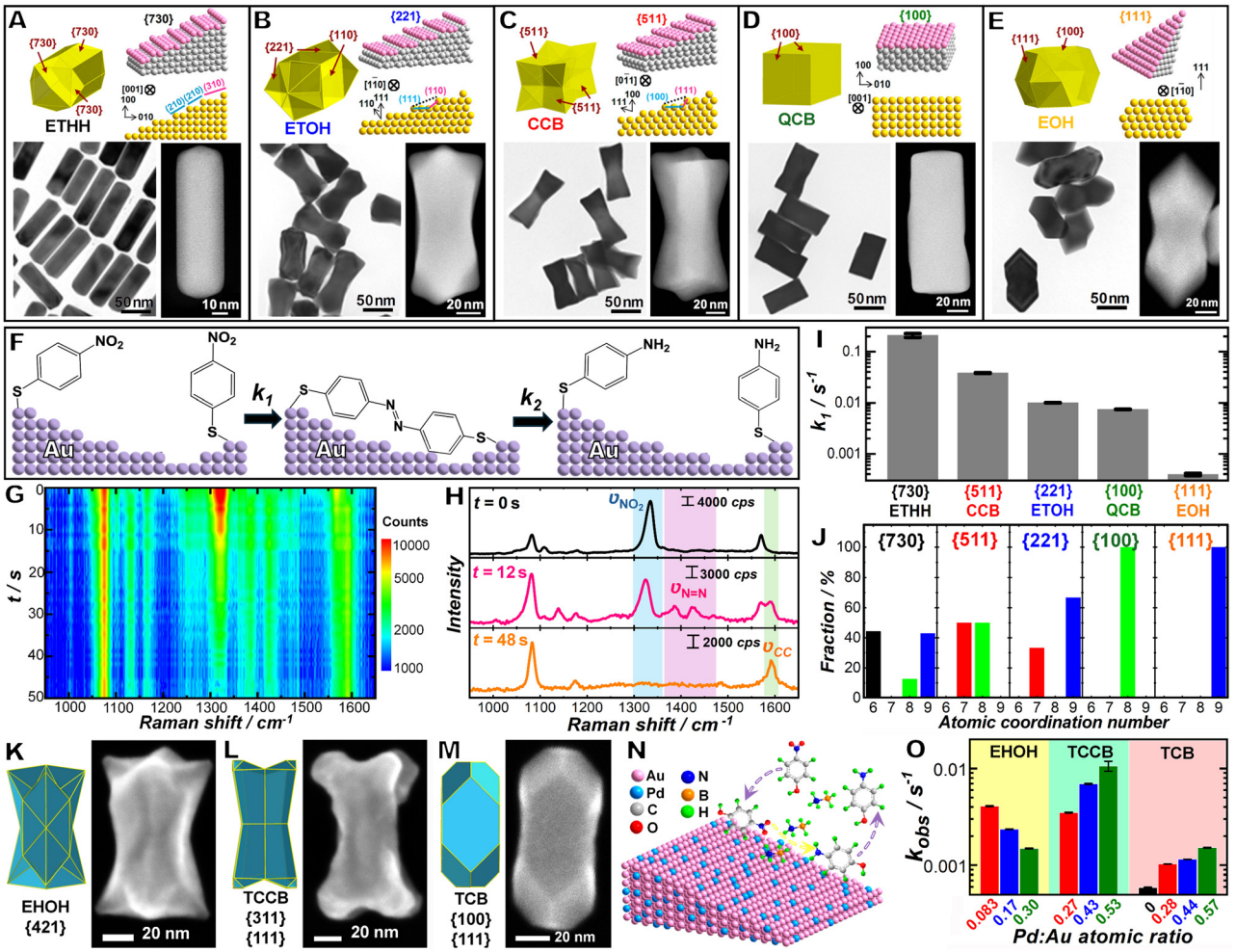


Fig. 5 Atomic-level surface structures (upper panels), TEM images (lower left panels), and high-angle annular dark-field scanning transmission electron microscopy (HAADF-STEM) images (lower right panels) of Au (A) ETHH, (B) ETOH, (C) CCB, (D) QCB, and (E) EOH nanoparticles. (F) Schematic illustration of catalytic transfer hydrogenation of pNTP adsorbates on Au surfaces. (G) Temporally evolving SERS spectra and (H) snapshot spectra collected at reaction times of 0, 12, and 48 s during the reactions after exposing pNTP-coated Au ETHH nanoparticles to 2 mM ammonia borane. (I) Apparent pseudo-first-order rate constants of the rate-limiting step ($k_1$) for the transfer hydrogenation reactions catalyzed by Au ETHH, ETOH, CCB, QCB, and EOH nanoparticles. (J) Fractions of surface atoms with various atomic coordination numbers for {730}, {511}, {221}, {100}, and {111} facets. Cartoon models (left panels) and SEM images (right panels) of individual Au–Pd alloy (K) EHOH, (L) TCCB, and (M) TCB nanoparticles. (N) Schematic illustration of the catalytic hydrogenation of nitrophenol by ammonia borane on an Au–Pd alloy surface. (O) Comparison of the apparent pseudo-first-order rate constants, $k_{obs}$, on EHOH, TCCB, and TCB alloy nanorods with various Pd/Au atomic ratios. Adapted with permission from (A)–(J) ref. 177 (Copyright 2016 American Chemical Society) and (K)–(O) ref. 179 (Copyright 2017 American Chemical Society).

allowing us to directly correlate the catalytic reaction rates with the facets exposed at the longitudinal ends of the nanorod-derived anisotropic nanoparticles. The reaction rate decreases in the order of {730} > {511} > {221} > {100} > {111} (Fig. 5(I)), revealing that lower CN of surface atoms results in higher catalytic activity for the transfer hydrogenation reaction (Fig. 5(J)).

Foreign ions other than $Cu^{2+}$ can also be used in conjunction with surface-capping surfactants to guide the structural evolution during nanorod overgrowth. When substituting $Cu^{2+}$ with $Ag^{+}$, metallic Ag may be either deposited as adatoms through underpotential deposition (UPD) or co-reduced together with Au to form alloys on nanorod surfaces.[178] The selective surface passivation by Ag UPD adlayers leads to the formation of high-index faceting dogbone-like nanorods with concave surface features, whereas the co-deposition of Au and Ag results in the formation of low-index faceting arrow-headed nanorods composed of Au–Ag alloys.[178] The two reaction pathways are interswitchable upon variation of the relative concentrations of $Ag^{+}$ ions, CTAB, and the reducing agent in the nanorod overgrowth solutions. Single-crystalline Au nanorods have also been used as the seeds to guide the co-deposition of Au and Pd to form Au–Pd alloy nanorods with well-defined facets. Deliberate kinetic control over the electroless deposition of Au–Pd alloy shells on Au nanorod seeds enables selective synthesis of a family of multifaceted Au–Pd bimetallic alloy nanostructures, including elongated hexoctahedral (EHOH) nanoparticles enclosed by 56 {*hkl*} high-index facets (Fig. 5(K)), truncated concave cuboidal (TCCB) nanoparticles

whose surfaces are dominated by 24 {*hkk*} high-index side facets with 8 truncated tips terminated by {111} facets (Fig. 5(L)), and truncated cuboidal (TCB) nanoparticles enclosed by {100} and {111} facets (Fig. 5(M)).[179] The seed-mediated co-reduction under diffusion-controlled conditions also enables the fine-tuning of the Au : Pd stoichiometric ratios in the alloy shells deposited on the Au nanorod seeds while well-preserving each multifaceted particle geometry. Both the surface atomic coordination and the compositional stoichiometries of the multi-faceted Au–Pd alloy nanorods are found to be key factors determining the overall rates of catalytic hydrogenation of *para*-nitrophenol by ammonia borane (Fig. 5(N) and (O)), a model reaction exhibiting the Langmuir–Hinshelwood kinetic features.

### 4.4. Implementing structural chirality in Au nanoparticles

Creation of structural chirality in Au nanostructures gives rise to the emergence of intriguing chiroptical activities and enantioselective catalytic properties. There are three basic ways to make achiral Au nanoparticles chiral: (1) coupling achiral Au nanoparticles with chiral molecular adsorbates;[180–184] (2) assembling achiral Au nanoparticles into chiral supranano-structures;[185–190] and (3) implementing structural chirality in individual Au nanoparticles.[191–194] Among the three types of chiral nanostrucutures, Au nanoparticles adopting intraparticle chiral geometries have been of particular interest because their functional chirality arises directly from their intrinsic structural chirality rather than indirectly from foreign molecular additives. Here, I focus on the most fundamental aspects concerning the development of structural chirality in colloidal Au nanocrystals, which are rooted in the enantioselective interactions between chiral molecular adsorbates and high-index crystallographic facets. The latest progress in the field of chiral plasmonic Au nanostructures regarding synthetic method development, structure–property relationships, and newly emerging applications in enantioselective catalysis, biosensing, and nanophotonics has been reviewed elsewhere in a series of recently published comprehensive review articles,[188,191–209] and therefore, is not further discussed in this feature article.

High-index facets of fcc Au have built-in structural chirality.[210–212] The absolute configurations of these chiral surfaces are determined by the spatial arrangement of the surface atoms at the kinked sites where low-index microfacets intersect. Chiral molecules can recognize and interact with the intrinsically chiral kinked sites on the high-index facets in an enantio-specific manner, resulting in nonequal crystal growth rates on the two oppositely chiral high-index planes. As a proof-of-concept, Nam and coworkers[213] successfully synthesized a series of single-crystalline chiral Au nanoparticles with helicoid morphologies that consist of highly twisted chiral elements. The synthetic methods for chiral Au nanohelicoids are similar to those developed for the high-index faceting Au nanocrystals in many aspects, except that chiral molecules, most commonly amino acids and peptides, are added to establish the enantioselective metal–adsorbate interactions.

In the absence of chiral molecular additives, single-crystalline Au nanocubes evolve into stellated octahedral nanocrystals, each of which is bound by 48 identical triangular high-index {321} facets with a 4/*m*2/*m* point group symmetry.[213] According to the rotational direction of the low-index microfacets, a {321} facet may adopt either the R (clockwise rotation, $\{321\}^{R}$) or the S (anticlockwise rotation, $\{32\bar{1}\}^{S}$) conformation. Cysteine, a chiral amino acid, can interact with {321} facets in an enantioselective manner, resulting in asymmetric overgrowth of the {321}-faceting Au nanocrystals. L-Cysteine adsorbs to the $\{321\}^{R}$ regions with higher affinity than to the $\{32\bar{1}\}^{S}$ regions, selectively slowing down the crystal growth on the R regions. Such enantioselective surface-passivation leads to the splitting of the boundaries between the $\{321\}^{R}$ and $\{32\bar{1}\}^{S}$ regions, tilting the boundaries preferentially toward the S region to form a chiral structure with the 432-point group symmetry, termed as Helicoid I (left panel in Fig. 6(A)). Similarly, adsorption of D-cysteine to the surfaces of the stellated Au nanooctahedra twists the boundaries toward the R region, producing Helicoid I structures with the opposite handedness (right panel in Fig. 6(A)). The left- and right-handed Helicoid I particles have essentially the same peak positions but inverted peak shapes in circular dichroism spectra (Fig. 6(B)).

Chiral molecular additives play crucial roles in guiding the growth of chiral Au nanocrystals. When L-glutathione (L-GSH) instead of L-cysteine or D-cysteine is added to the overgrowth solution, Au nanocubes evolve into a strikingly different chiral morphology with the same 432 point group symmetry, referred to as Helicoid II (Fig. 6(C)), by twisting a different *R*–*S* boundary between $\{312\}^{R}$ and $\{312\}^{S}$.[213] Under the same overgrowth conditions, switching the seed particles from Au nanocubes to Au nanooctahedra leads to the formation of another type of chiral nanostructures, denoted as Helicoid III, without changing the 432 point group symmetry of the particles. Each Helicoid III nanoparticle exhibits a pinwheel-like morphology consisting of four highly curved arms on each of the six faces of the cubic geometry (Fig. 6(D)).[213] In comparison to Helicoids I and II, the chiral elements in Helicoid III are twisted with a higher curvature and the grooves between the twisted ridges are deeper, resulting in even stronger optical activity with dissymmetry factors (*g*-factors) significantly larger than those of Helicoids I and II.

Over the past few years, a large library of structurally distinct Au nanocrystals with intrinsic structural chirality have been successfully synthesized choosing structurally tailored Au nanocrystals as the seeds and a diverse range of chiral molecules as the structure-directing agents. For example, a pentatwinned Au nanododecahedron with 5-fold rotational symmetry evolves into a chiral pentagonal nanostar (PNS) and a chiral pentagonal nanoprism (PNP) when using CYP (cysteine–phenylalanine) and GSH (γ-glutamic acid–cysteine–glycine) as chirality-inducers, respectively (Fig. 6(E)).[214] Employing achiral single-crystalline Au nanorods as the seeds, a series of quasi-one-dimensional chiral Au nanostructures with tunable aspect ratios and controlled handedness can be synthesized (Fig. 6(F)–(H)).[215–217] Quasi-two-dimensional chiral Au nanostructures have also been synthesized through deliberately designed colloidal or surface-guided nanocrystal overgrowth processes. For example, Au nanopropellers (Fig. 6(I)) can be derived

 

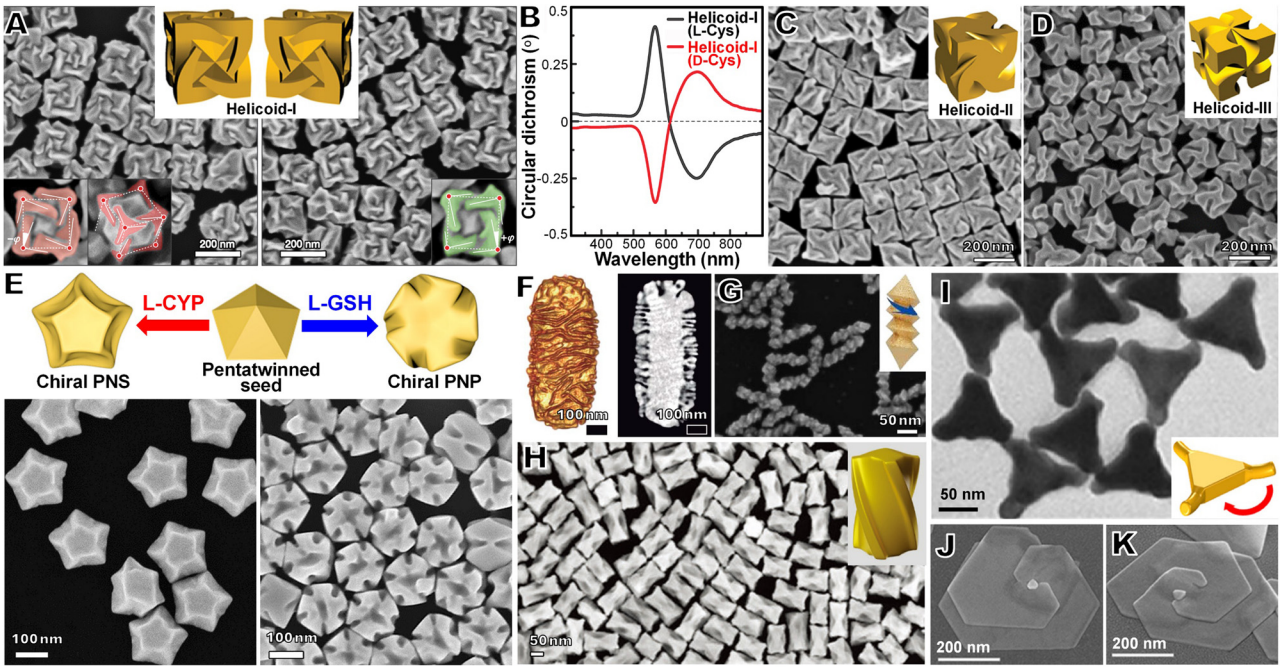


Fig. 6 (A) SEM images and (B) circular dichroism spectra of Au Helicoid-I nanoparticles with two different handedness. SEM images of Au (C) Helicoid-II and (D) Helicoid-III nanoparticles. (E) Schematic illustration of particle synthesis (upper panel) and SEM images of chiral PNS (lower left panel) and PNP (lower right panel) particles. (F) Tomography reconstruction (left panel) and HAADF-STEM image (right panel) of chiral Au nanorods synthesized through micelle-directed chiral seeded growth. (G) SEM image of helical Au nanorods. (H) SEM image of fourfold twisted Au nanorods. (I) TEM image of Au nanopropellers. (J) and (K) SEM images of Au nanospirals. Adapted with permission from (A)–(D) ref. 213 (Copyright 2018 Springer Nature), (E) ref. 214 (Copyright 2024 American Chemical Society), (F) ref. 215 (Copyright 2020 American Association for the Advancement of Science), (G) ref. 216 (Copyright 2021 American Chemical Society), (H) ref. 217 (Copyright 2023 John Wiley and Sons), (I) ref. 218 (Copyright 2020 American Chemical Society), and (J) and (K) ref. 219 (Copyright 2021 American Chemical Society).

from cysteine-guided overgrowth of achiral Au nanoprims.[218] Au nanospirals (Fig. 6(J) and (K)) can be synthesized through plasmon-driven asymmetric growth of surface-immobilized seeds using protonated phenyl-modified carbon nitride as a chirality-inducer.[219] Regardless of how complicated the targeted chiral nanostructures are, three most critical factors much be taken into careful consideration when designing synthetic approaches to chiral Au nanostructures. First, the nanocrystal overgrowth conditions must be controlled to favor the formation of specific types of high-index facets or atomically kinked surface sites with intrinsic structural chirality. Second, the choice of chiral molecular additives should ensure effective transfer of the molecular chirality to the chiral growth of nanocrystals. Third, the structures of the Au seeds need to be judiciously tailored to promote the chiral twist at the boundaries between targeted facets. These guiding principles provide the keystone for designing synthetic approaches to chiral Au nanostructures with targeted chiroptical and enantioselective catalytic functions. The library of experimentally realizable Au chiral nanostructures will continue to expand rapidly, as there seem to be an unlimited number of combinations of seed structures, chiral molecular additives, and nanocrystal overgrowth environments one can choose for chiral nanostructure synthesis.

### 4.5. Tuning interband transitions in Au-based nanostructures

The tunable light absorption and scattering properties of Au nanoparticles in the visible and NIR spectral regions are essentially determined by the behaviors of free electrons in the conduction band (6sp band in the case of Au), purely plasmonic in nature. Au nanoparticles also absorb light on the higher-energy (shorter-wavelength) side of their plasmon resonances due to electronic interband transitions.[220] As schematically illustrated in Fig. 7(A), the interband transitions of electrons in Au from the 5d to 6sp bands occur when the excitation photon energy exceeds a threshold of ~2.3 eV (~538 nm). Photoexcitations of d-to-sp interband electronic transitions in Au result in generation of hot holes in the d band below the Fermi level and hot electrons in the sp band near the Fermi level.[13,220] In contrast to the interband transitions, resonantly excited localized plasmons in Au nanoparticles, in the context of the classical electromagnetic theory, can be described as collective oscillations of free electrons in the 6sp band in response to the electric fields of the excitation light. The plasmon resonances may decay nonradiatively into non-thermal hot electrons and holes within the 6sp band of Au.[11,13] The hot electrons can be distributed within an energy range from $E_F$ to $E_F + \hbar\omega$ ($E_F$ is the Fermi energy of Au and $\hbar\omega$ is the energy of an excitation photon), while the hot holes reside below $E_F$. In a quantum mechanical description, resonant excitations of localized plasmons involve electronic transitions between sp-band states with different electron momenta and are thus, also called intraband electronic excitations.[10,13] Both the interband hot carriers derived from the d-to-sp interband transitions and the intraband hot carriers derived from

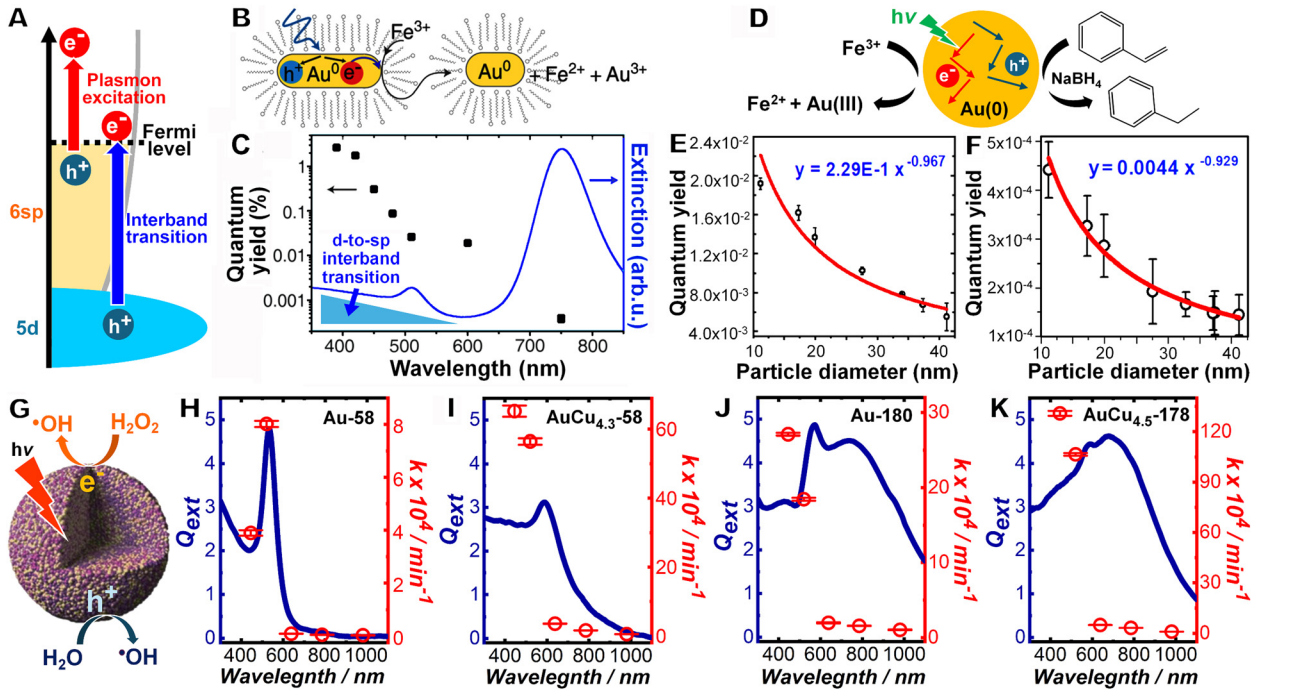


Fig. 7 (A) Photoexcitation of interband and intraband hot carriers in Au. (B) Schematic illustration of photo-enhanced etching of Au nanorods by $Fe^{3+}$. (C) Quantum yield of the Au etching reaction at various excitation wavelengths, with reference to the optical extinction spectra of Au nanorods. (D) Schematic illustration of hot carrier-driven etching of Au nanoparticles and reduction of styrene. Particle size-dependent quantum yields for (E) the etching of Au nanoparticles under interband excitations (440 nm, 13.7 mW) and (F) the reduction of styrene under interband excitations (405 nm, 415 mW). (G) Schematic illustration of hot carrier-driven generation of •OH radicals catalyzed by an Au–Cu alloy nanoparticle. Experimentally measured extinction spectra of various Au and Au–Cu alloy nanoparticle samples and the apparent rate constants of photocatalytic RhB degradation at various excitation wavelengths in the presence of 2 mM $H_2O_2$ and (H) Au-58, (I) $AuCu_{4.3}$-58, (J) Au-180, and (K) $AuCu_{4.5}$-178 nanoparticles. The concentration of colloidal nanoparticles in the reactant mixtures was kept at $\sim 1.0 \times 10^9$ particles $mL^{-1}$. The excitation power at various excitation wavelengths were fixed at 0.5 W. Adapted with permission from (B) and (C) ref. 224 (Copyright 2017 American Chemical Society), (D)–(F) ref. 226 (Copyright 2019 American Chemical Society), and (G)–(K) ref. 230 (Copyright 2024 American Chemical Society).

plasmon decay are exploitable for photocatalysis. However, these two types of photoexcited hot carriers in Au nanoparticles differ strikingly from each other in terms of energy distributions, relaxation dynamics, and diffusion lengths, and therefore may exhibit remarkably different photocatalytic behaviors.[220–223]

Oxidative etching of Au nanorods by $Fe^{3+}$ cations has been a model reaction ideal for comparing the photocatalytic efficacies of the interband and intraband hot carriers photogenerated in Au.[224] As illustrated in Fig. 7(B), $Fe^{3+}$ cations can oxidize metallic Au to produce Au(III) ions preferentially at the ends of Au nanorods, which leads to shortening of Au nanorods and a spectral blue-shift of the longitudinal plasmon band. The etching of Au nanorods is kinetically very slow in the dark but becomes significantly faster under light illumination due to photogeneration of either intraband or interband hot carriers in Au nanorods. The hot carriers are more abundant at the ends than at the lateral sides of Au nanorods, promoting the regioselective Au dissolution at the ends of Au nanorods under both chemical and electrochemical etching conditions.[224,225] The longitudinal plasmon resonance of Au nanorods can be shifted into the NIR region, far below the energy threshold for interband transitions, whereas the transverse plasmon resonances spectrally overlap with the tail of the interband absorption. The wavelength-dependence of quantum yields, *i.e.* the action spectrum of photocatalysis, shown in Fig. 7(C) reveals that the interband hot carriers are drastically more efficient in catalyzing the etching of Au nanorods. The quantum yield of the interband hot carrier-driven reactions becomes higher as the excitation wavelength decreases. Although the longitudinal plasmon peak is far more intense than the transverse plasmon peak in the extinction spectrum, photoexcitations at the transverse plasmon resonance wavelengths result in much higher quantum yields than at the longitudinal plasmon resonance wavelengths due to the contribution of interband transitions. These results indicate that interband transitions can more efficiently generate hot carriers exploitable for oxidative etching of Au nanorods than intraband excitations of localized plasmons. A similar trend has also been observed in the Au nanoparticle-catalyzed cyclization reaction of alkynylphenols.[224]

Only a small fraction of the photoexcited hot carriers can be extracted from Au nanoparticles and become exploitable for photocatalysis. The size of Au nanoparticles has been found to be a critical factor determining the excitation and utilization efficiencies of hot carriers.[226] The scattering-to-absorption ratio increases with the size of Au nanoparticles. Smaller Au nanoparticles are stronger light absorbers at their plasmon resonance frequencies, and are thus considered more efficient

 

in generating plasmonic hot carriers in comparison to larger Au nanoparticles. To become exploitable for photocatalysis, the energetic hot carriers must migrate to the nanoparticle surfaces and get transferred to surface-adsorbed molecules or ions before they are relaxed and thermalized within the metal lattices. Choosing chemical etching of Au nanoparticles by $Fe^{3+}$ and transfer hydrogenation of styrene (Fig. 7(D)) as model reactions, Nguyen and coworkers[226] have demonstrated that the diffusion of photoexcited hot carriers inside Au nanoparticles is a critical factor limiting the surface abundance and utilization efficiencies of hot carriers for photocatalysis. For both reactions, Au nanoparticles are photocatalytically more active under interband excitations than under plasmonic excitations. The apparent reaction rates decrease as the size of Au nanoparticles increases. The quantum yields under interband excitations are proportional to the reciprocal of the particle size (Fig. 7(E) and (F)), a characteristic scaling law rooted in the intraparticle diffusion of photoexcited hot carriers. Under plasmon excitation conditions, however, the size-dependent photocatalytic activity of Au nanoparticles deviates slightly from this scaling law, possibly due to the influence by the local-field enhancements on the nanoparticle surfaces.

Although the plasmon resonance frequencies of Au nanoparticles can be systematically tuned over a broad spectral range across the visible and infrared regions, interband transitions in Au nanoparticles can only be excited within an essentially fixed spectral window ranging from the ultraviolet to the blue region of the visible spectrum, independent of the particle geometries and local environments.[220] The spectral range in which interband transitions occur is essentially determined by the electronic band structures of Au. The electronic states in an Au nanoparticle are considered as continuous and metal-like, analogous to those in bulk Au materials, as long as the nanoparticle is larger than a few nanometers, *i.e.*, in the plasmonically relevant size regime. The onset of interband transitions in Au nanoparticles is around 2.3 eV, which corresponds to the energy gap between the edge of the d band and the Fermi level of Au. Tuning the onset of interband transitions requires modification of the d band energy with respect to the Fermi level, which can be achieved by alloying Au with transition noble metals, such as Pd. As demonstrated by McPeak and coworkers,[227] $Au_xPd_{1-x}$ alloy films, under NIR excitations at 1550 nm (the optical fiber wavelength), can provide up to a 20-fold increase in the number of hot carriers in comparison to their monometallic Au counterparts with carrier lifetimes about 3 times longer than those in monometallic Pd films. As shown more recently by Ross and coworkers,[228,229] incorporating post-transition metal elements, such as Sn, In, and Bi, into the Au lattice can shift the onset of interband transitions with respect to the plasmon resonance wavelengths, which enables modulation of plasmon damping caused by interband transitions. How the spectral overlap between plasmon resonances and interband transitions affects the photocatalytic efficacies of interband and intraband hot carriers remains a fundamentally interesting open question.

Au–Cu alloy nanoparticles represent a unique material system, in which the excitation energy threshold for d-to-sp interband transitions becomes tunable upon variation of Cu/Au stoichiometric ratios, while the plasmon resonance frequency can be tuned by changing the particle sizes.[230] The degree of spectral overlap between interband transitions and plasmon resonances in the visible region not only regulates the damping of plasmon resonances but also profoundly influences the photocatalytic efficacies of intraband and interband hot carriers in Au–Cu alloy nanoparticles. As illustrated in Fig. 7(G), both the intraband and interband hot electrons photoexcited in Au–Cu alloy nanoparticles can be harnessed to drive the reduction of $H_2O_2$, which produces $^{\bullet}OH$ radicals. Alternatively, $^{\bullet}OH$ radicals can be produced through interband hot hole-driven oxidation of $H_2O$. The $^{\bullet}OH$ radicals derived from interband and intraband hot carrier-driven reactions are highly reactive, capable of degrading dye molecules, such as Rhodamine B (RhB), in aqueous environments. When using relatively small Au nanoparticles (average diameter of 58 nm, denoted as Au-58) within the quasi-static limit as the photocatalysts for RhB degradation in the presence of $H_2O_2$, the action spectrum matches the extinction spectral profiles of the nanoparticles very well (Fig. 7(H)). However, alloying Au with Cu in similar-sized nanoparticles ($AuCu_{4.3}$ alloy nanoparticles with an average diameter of 58 nm, denoted as AuCu-58) leads to remarkably enhanced photocatalysis under interband excitations, and the photocatalytic action spectrum deviates significantly from the optical extinction spectra (Fig. 7(I)). In larger nanoparticles beyond the quasi-static limit, the interband hot carriers have been observed to be photocatalytically more active than the intraband plasmonic hot carriers in both monometallic Au (Fig. 7(J)) and Au–Cu alloy nanoparticles (Fig. 7(K)). With similar particle sizes around 180 nm, $AuCu_{4.5}$ alloy nanoparticles (denoted as $AuCu_{4.5}$-178) appear photocatalytically far more efficient than their monometallic counterparts (denoted as Au-180) under interband excitations. At a fixed Cu/Au stoichiometric ratio, the surface-specific rate constants of the photocatalytic reactions driven by intraband hot carriers decay more rapidly than those of interband hot carrier-driven reactions as the particle size increases, suggesting that the interband hot carriers may have longer lifetimes and diffusion lengths in comparison to the intraband hot carriers. At a given particle size, the photocatalytic reactions become kinetically faster upon increase of the Cu/Au stoichiometric ratio in the alloy nanoparticles under interband excitations, which can be most reasonably interpreted in the context of composition-dependent hot carrier lifetimes as well as the energy shift of the d band and Fermi level. These results indicate that the particle dimensions and compositional stoichiometries are both key factors influencing the photocatalytic efficacies of interband and intraband hot carriers in Au-based alloy nanoparticles.

## 5. Conclusions and outlook

In this feature article, I have elucidated the detailed structure–property relationships underpinning the integrated optical and

catalytic tunabilities of several deliberately designed Au-based nanostructures, including surface-roughened Au nanoparticles, dealloyed Au nanosponges, high-index faceting Au nanorods, and chiral Au nanocrystals. Although experimental realization of the above-mentioned nanostructures relies on seemingly diverse synthetic approaches, the basic strategies for integrating tunable optical and catalytic properties in single Au nanostructures inevitably involve precise control of the atomic-level surface structures of Au nanoparticles whose dimensions are in the plasmonically relevant, subwavelength size regime. Merging plasmonic and catalytic tunabilities within the same nanoscale entities creates unique opportunities to use plasmon-enhanced spectroscopies, such as SERS, as *in situ* molecule-fingerprinting tools to precisely monitor detailed structural evolution of molecular adsorbates in real time during catalytic reactions. Au nanoparticles with finely optimizable plasmonic-catalytic dual-functionalities also provide a unique material platform, based upon which various plasmon-derived photophysical and photochemical effects can be harnessed to drive or enhance catalytic molecule-transforming processes. Alloying Au with other metal elements in nanoparticles further enables us to tune the degree of spectral overlap between interband transitions and plasmon resonances, which profoundly influences not only the damping of plasmons but also the photocatalytic behaviors of intraband and interband hot carriers. Success in precise tuning of both the optical and catalytic properties of Au-based nanostructures provides a solid foundation for us to further answer a series of fundamentally important and challenging scientific questions at the interface between nanoplasmonics and nanocatalysis.

All the Au-based nanostructures discussed so far in this feature article, regardless of how complicated their particle geometries are, form the fcc crystalline lattices. It has been recently observed that non-fcc lattices may also emerge in Au nanostructures under specific synthetic conditions.[231–234] The unconventional non-fcc Au nanostructures may become even more active in catalyzing certain reactions than their counterparts adopting the conventional fcc structures.[231–233] The non-fcc Au nanocrystals typically exhibit exotic anisotropic particle geometries with intrinsic plasmonic tunability. In the case of non-fcc Au nanostructures, the design principles of synthetic methods and the structure–property relationships may differ vastly from those applicable to the fcc Au nanoparticles. How to fine-tune the optical and catalytic properties simultaneously within the same non-fcc Au nanoparticles remains a fundamentally intriguing topic well-worthy of further investigations.

The surfaces of virtually all experimentally synthesized colloidal Au nanoparticles are capped with molecular ligands, which play crucial roles in guiding the structural evolution of Au nanocrystals during colloidal synthesis. Surface-adsorbed ligand molecules may cause a spectral shift of the plasmon resonance bands by changing the local dielectric environments surrounding the nanoparticles. When the adsorbate orbitals are strongly coupled Au plasmons, the spectral lineshapes of plasmon resonance bands can be significantly modified due to chemical interface damping, which involves direct injection of hot carriers in molecular adsorbates.[235,236] On the other hand, molecular adsorbates may modify the intrinsic catalytic properties of the Au nanoparticles by influencing the interactions of reactant molecules with the active sites on Au surfaces.[237–241] How molecular adsorbates affect the intrinsic physicochemical properties of plasmonic-catalytic dual-functional Au-based nanostructures deserves further investigations in greater detail at a higher level of quantitativeness.

Au-based nanostructures may function as plasmonic resonators and active catalysts simultaneously, and have thereby been widely used for plasmon-mediated photocatalysis. Several plasmon-derived effects, including nonthermal hot carriers, local-field enhancements, and photothermal transduction, can all play crucial roles in determining the overall kinetic features of photocatalytic reactions.[10–12,242–252] It has long been challenging to distinguish and quantify the contributions of multiple intertwining effects to plasmonic photocatalysis, especially for mechanistically complex reactions involving multiple reaction pathways. The exact roles of nonthermal *vs.* thermal effects,[253–257] Landau damping *vs.* chemical interface damping,[258,259] and local-field enhancements *vs.* hot carrier transfer[260] in various plasmon-mediated photocatalytic reactions have been widely debated. Success in developing an in-depth mechanistic understanding of plasmonic photocatalysis not only requires development of time-resolved and steady-state spectroscopic and computational tools but also ultimately relies on precise structural control of plasmonic-catalytic dual-functional nanoparticles.

## Author contributions

Single author contribution.

## Conflicts of interest

There are no conflicts to declare.

## Data availability

No primary research results, software or code have been included and no new data were generated or analyzed as part of this feature article.

## Acknowledgements

The author acknowledges the funding support provided by the National Science Foundation (NSF) of the United States of America under Grants CHE-2202928, DMR-1253231, and OIA-1655740. The content is solely the responsibility of the author and does not necessarily represent the official views of the NSF. The publication cost of this article is covered by the University of South Carolina Libraries Open Access Fund.

## Notes and references

1 E. Hutter and J. H. Fendler, *Adv. Mater.*, 2004, **16**, 1685–1706.
2 S. Eustis and M. A. El-Sayed, *Chem. Soc. Rev.*, 2006, **35**, 209–217.

 

3 S. Lal, S. Link and N. J. Halas, *Nat. Photonics*, 2007, **1**, 641–648.
4 K. A. Willets and R. P. Van Duyne, *Annu. Rev. Phys. Chem.*, 2007, **58**, 267–297.
5 P. K. Jain, X. H. Huang, I. H. El-Sayed and M. A. El-Sayed, *Acc. Chem. Res.*, 2008, **41**, 1578–1586.
6 N. J. Halas, S. Lal, W. S. Chang, S. Link and P. Nordlander, *Chem. Rev.*, 2011, **111**, 3913–3961.
7 G. V. Hartland, *Chem. Rev.*, 2011, **111**, 3858–3887.
8 K. M. Mayer and J. H. Hafner, *Chem. Rev.*, 2011, **111**, 3828–3857.
9 S. Link and M. A. El-Sayed, *J. Phys. Chem. B*, 1999, **103**, 8410–8426.
10 M. L. Brongersma, N. J. Halas and P. Nordlander, *Nat. Nanotechnol.*, 2015, **10**, 25–34.
11 Y. C. Zhang, S. He, W. X. Guo, Y. Hu, J. W. Huang, J. R. Mulcahy and W. D. Wei, *Chem. Rev.*, 2018, **118**, 2927–2954.
12 M. J. Kale, T. Avanesian and P. Christopher, *ACS Catal.*, 2014, **4**, 116–128.
13 A. O. Govorov, H. Zhang, H. V. Demir and Y. K. Gun'ko, *Nano Today*, 2014, **9**, 85–101.
14 M. G. Blaber, M. D. Arnold and M. J. Ford, *J. Phys.: Condens. Matter*, 2010, **22**, 143201.
15 G. V. Naik, V. M. Shalaev and A. Boltasseva, *Adv. Mater.*, 2013, **25**, 3264–3294.
16 M. W. Knight, L. F. Liu, Y. M. Wang, L. Brown, S. Mukherjee, N. S. King, H. O. Everitt, P. Nordlander and N. J. Halas, *Nano Lett.*, 2012, **12**, 6000–6004.
17 M. W. Knight, N. S. King, L. F. Liu, H. O. Everitt, P. Nordlander and N. J. Halas, *ACS Nano*, 2014, **8**, 834–840.
18 J. S. Biggins, S. Yazdi and E. Ringe, *Nano Lett.*, 2018, **18**, 3752–3758.
19 Y. Zhao, H. Pan, Y. Lou, X. Qiu, J. Zhu and C. Burda, *J. Am. Chem. Soc.*, 2009, **131**, 4253–4261.
20 J. M. Luther, P. K. Jain, T. Ewers and A. P. Alivisatos, *Nat. Mater.*, 2011, **10**, 361–366.
21 D. Dorfs, T. Härtling, K. Miszta, N. C. Bigall, M. R. Kim, A. Genovese, A. Falqui, M. Povia and L. Manna, *J. Am. Chem. Soc.*, 2011, **133**, 11175–11180.
22 I. Kriegel, C. Jiang, J. Rodríguez-Fernández, R. D. Schaller, D. V. Talapin, E. da Como and J. Feldmann, *J. Am. Chem. Soc.*, 2012, **134**, 1583–1590.
23 Y. Xie, A. Riedinger, M. Prato, A. Casu, A. Genovese, P. Guardia, S. Sottini, C. Sangregorio, K. Miszta, S. Ghosh, T. Pellegrino and L. Manna, *J. Am. Chem. Soc.*, 2013, **135**, 17630–17637.
24 I. Kriegel, J. Rodríguez-Fernández, A. Wisnet, H. Zhang, C. Waurisch, A. Eychmüller, A. Dubavik, A. O. Govorov and J. Feldmann, *ACS Nano*, 2013, **7**, 4367–4377.
25 M. Sun, X. Fu, K. Chen and H. Wang, *ACS Appl. Mater. Interfaces*, 2020, **12**, 46146–46161.
26 M. Sun, N. Kreis, K. Chen, X. Fu, S. Guo and H. Wang, *Chem. Mater.*, 2021, **33**, 8546–8558.
27 M. Sun, Z. Wang and H. Wang, *Chem. Mater.*, 2022, **34**, 1965–1975.
28 K. Manthiram and A. P. Alivisatos, *J. Am. Chem. Soc.*, 2012, **134**, 3995–3998.
29 X. C. Ye, J. Y. Fei, B. T. Diroll, T. Paik and C. B. Murray, *J. Am. Chem. Soc.*, 2014, **136**, 11680–11686.
30 R. Buonsanti, A. Llordes, S. Aloni, B. A. Helms and D. J. Milliron, *Nano Lett.*, 2011, **11**, 4706–4710.
31 M. Kanehara, H. Koike, T. Yoshinaga and T. Teranishi, *J. Am. Chem. Soc.*, 2009, **131**, 17736–17737.
32 S. D. Lounis, E. L. Runnerstrom, A. Bergerud, D. Nordlund and D. J. Milliron, *J. Am. Chem. Soc.*, 2014, **136**, 7110–7116.
33 T. R. Gordon, T. Paik, D. R. Klein, G. V. Naik, H. Caglayan, A. Boltasseva and C. B. Murray, *Nano Lett.*, 2013, **13**, 2857–2863.
34 Z. Liu, Y. Zhong, I. Shafei, S. Jeong, L. Wang, H. T. Nguyen, C.-J. Sun, T. Li, J. Chen, L. Chen, Y. Losovyj, X. Gao, W. Ma and X. Ye, *Nano Lett.*, 2020, **20**, 2821–2828.
35 H. Bai, S. H. Lam, J. Yang, X. Cheng, S. Li, R. Jiang, L. Shao and J. Wang, *Adv. Mater.*, 2022, **34**, 2104226.
36 P. K. B. Palomaki, E. M. Miller and N. R. Neale, *J. Am. Chem. Soc.*, 2013, **135**, 14142–14150.
37 S. Askari, D. Mariotti, J. E. Stehr, J. Benedikt, J. Keraudy and U. Helmersson, *Nano Lett.*, 2018, **18**, 5681–5687.
38 G. Manna, R. Bose and N. Pradhan, *Angew. Chem., Int. Ed.*, 2013, **52**, 6762–6766.
39 L. De Trizio, R. Gaspari, G. Bertoni, I. Kriegel, L. Moretti, F. Scotognella, L. Maserati, Y. Zhang, G. C. Messina, M. Prato, S. Marras, A. Cavalli and L. Manna, *Chem. Mater.*, 2015, **27**, 1120–1128.
40 Y. N. Xia and N. J. Halas, *MRS Bull.*, 2005, **30**, 338–344.
41 S. E. Skrabalak, J. Y. Chen, Y. G. Sun, X. M. Lu, L. Au, C. M. Cobley and Y. N. Xia, *Acc. Chem. Res.*, 2008, **41**, 1587–1595.
42 E. C. Dreaden, A. M. Alkilany, X. H. Huang, C. J. Murphy and M. A. El-Sayed, *Chem. Soc. Rev.*, 2012, **41**, 2740–2779.
43 S. E. Lohse and C. J. Murphy, *Chem. Mater.*, 2013, **25**, 1250–1261.
44 J. E. Millstone, S. J. Hurst, G. S. Métraux, J. I. Cutler and C. A. Mirkin, *Small*, 2009, **5**, 646–664.
45 M. Grzelczak, J. Pérez-Juste, P. Mulvaney and L. M. Liz-Marzán, *Chem. Soc. Rev.*, 2008, **37**, 1783–1791.
46 L. L. Zhang, M. X. Zhou, A. Q. Wang and T. Zhang, *Chem. Rev.*, 2020, **120**, 683–733.
47 G. Li and R. C. Jin, *Acc. Chem. Res.*, 2013, **46**, 1749–1758.
48 T. V. W. Janssens, B. S. Clausen, B. Hvolbæk, H. Falsig, C. H. Christensen, T. Bligaard and J. K. Norskov, *Top. Catal.*, 2007, **44**, 15–26.
49 T. Ishida, T. Murayama, A. Taketoshi and M. Haruta, *Chem. Rev.*, 2020, **120**, 464–525.
50 B. Hvolbaek, T. V. W. Janssens, B. S. Clausen, H. Falsig, C. H. Christensen and J. K. Norskov, *Nano Today*, 2007, **2**, 14–18.
51 M. Haruta, *CATTECH*, 2002, **6**, 102–115.
52 A. Haruta, *Chem. Rec.*, 2003, **3**, 75–87.
53 A. Corma and H. Garcia, *Chem. Soc. Rev.*, 2008, **37**, 2096–2126.
54 M. D. Hughes, Y. J. Xu, P. Jenkins, P. McMorn, P. Landon, D. I. Enache, A. F. Carley, G. A. Attard, G. J. Hutchings, F. King, E. H. Stitt, P. Johnston, K. Griffin and C. J. Kiely, *Nature*, 2005, **437**, 1132–1135.
55 M. Valden, X. Lai and D. W. Goodman, *Science*, 1998, **281**, 1647–1650.
56 X. F. Yang, A. Q. Wang, B. T. Qiao, J. Li, J. Y. Liu and T. Zhang, *Acc. Chem. Res.*, 2013, **46**, 1740–1748.
57 M. Turner, V. B. Golovko, O. P. H. Vaughan, P. Abdulkin, A. Berenguer-Murcia, M. S. Tikhov, B. F. G. Johnson and R. M. Lambert, *Nature*, 2008, **454**, 981–983.
58 E. Roduner, *Chem. Soc. Rev.*, 2006, **35**, 583–592.
59 A. A. Herzing, C. J. Kiely, A. F. Carley, P. Landon and G. J. Hutchings, *Science*, 2008, **321**, 1331–1335.
60 M. S. Chen and D. W. Goodman, *Science*, 2004, **306**, 252–255.
61 M. Haruta, T. Kobayashi, H. Sano and N. Yamada, *Chem. Lett.*, 1987, 405–408.
62 H. F. Qian, M. Z. Zhu, Z. K. Wu and R. C. Jin, *Acc. Chem. Res.*, 2012, **45**, 1470–1479.
63 K. Kwak and D. Lee, *Acc. Chem. Res.*, 2019, **52**, 12–22.
64 J. Langer, D. J. de Aberasturi, J. Aizpurua, R. A. Alvarez-Puebla, B. Auguie, J. J. Baumberg, G. C. Bazan, S. E. J. Bell, A. Boisen, A. G. Brolo, J. Choo, D. Cialla-May, V. Deckert, L. Fabris, K. Faulds, F. J. G. de Abajo, R. Goodacre, D. Graham, A. J. Haes, C. L. Haynes, C. Huck, T. Itoh, M. Ka, J. Kneipp, N. A. Kotov, H. Kuang, E. C. Le Ru, H. K. Lee, J. F. Li, X. Y. Ling, S. A. Maier, T. Mayerhofer, M. Moskovits, K. Murakoshi, J. M. Nam, S. Nie, Y. Ozaki, I. Pastoriza-Santos, J. Perez-Juste, J. Popp, A. Pucci, S. Reich, B. Ren, G. C. Schatz, T. Shegai, S. Schlucker, L. L. Tay, K. G. Thomas, Z. Q. Tian, R. P. Van Duyne, T. Vo-Dinh, Y. Wang, K. A. Willets, C. Xu, H. Xu, Y. Xu, Y. S. Yamamoto, B. Zhao and L. M. Liz-Marzán, *ACS Nano*, 2020, **14**, 28–117.
65 S. Y. Ding, J. Yi, J. F. Li, B. Ren, D. Y. Wu, R. Panneerselvam and Z. Q. Tian, *Nat. Rev. Mater.*, 2016, **1**, 16021.
66 S. Schlücker, *Angew. Chem., Int. Ed.*, 2014, **53**, 4756–4795.
67 C. F. Bohren and D. R. Huffman, *Absorption and Scattering of Light by Small Particles*, Wiley-VCH Verlag GmbH & Co. KGaA, 1998.
68 N. G. Bastús, J. Comenge and V. Puntes, *Langmuir*, 2011, **27**, 11098–11105.
69 C. Ziegler and A. Eychmüller, *J. Phys. Chem. C*, 2011, **115**, 4502–4506.
70 P. Zhang, Y. Li, D. Wang and H. Xia, *Part. Part. Syst. Charact.*, 2016, **33**, 924–932.
71 X. C. Ye, L. H. Jin, H. Caglayan, J. Chen, G. Z. Xing, C. Zheng, V. Doan-Nguyen, Y. J. Kang, N. Engheta, C. R. Kagan and C. B. Murray, *ACS Nano*, 2012, **6**, 2804–2817.
72 X. C. Ye, C. Zheng, J. Chen, Y. Z. Gao and C. B. Murray, *Nano Lett.*, 2013, **13**, 765–771.
73 A. Gole and C. J. Murphy, *Chem. Mater.*, 2004, **16**, 3633–3640.

74 L. Scarabelli, A. Sánchez-Iglesias, J. Pérez-Juste and L. M. Liz-Marzán, *J. Phys. Chem. Lett.*, 2015, **6**, 4270–4279.
75 B. Nikoobakht and M. A. El-Sayed, *Chem. Mater.*, 2003, **15**, 1957–1962.
76 L. Vigderman and E. R. Zubarev, *Chem. Mater.*, 2013, **25**, 1450–1457.
77 K. Park, L. F. Drummy, R. C. Wadams, H. Koerner, D. Nepal, L. Fabris and R. A. Vaia, *Chem. Mater.*, 2013, **25**, 555–563.
78 G. González-Rubio, V. Kumar, P. Llombart, P. Díaz-Núñez, E. Bladt, T. Altantzis, S. Bals, O. Peña-Rodríguez, E. G. Noya, L. G. MacDowell, A. Guerrero-Martínez and L. M. Liz-Marzán, *ACS Nano*, 2019, **13**, 4424–4435.
79 J. P. Zheng, X. Z. Cheng, H. Zhang, X. P. Bai, R. Q. Ai, L. Shao and J. F. Wang, *Chem. Rev.*, 2021, **121**, 13342–13453.
80 M. Z. Liu and P. Guyot-Sionnest, *J. Phys. Chem. B*, 2005, **109**, 22192–22200.
81 A. Sánchez-Iglesias, N. Winckelmans, T. Altantzis, S. Bals, M. Grzelczak and L. M. Liz-Marzán, *J. Am. Chem. Soc.*, 2017, **139**, 107–110.
82 Q. Li, X. L. Zhuo, S. Li, Q. F. Ruan, Q. H. Xu and J. F. Wang, *Adv. Opt. Mater.*, 2015, **3**, 801–812.
83 T. H. Chow, N. N. Li, X. P. Bai, X. L. Zhuo, L. Shao and J. F. Wang, *Acc. Chem. Res.*, 2019, **52**, 2136–2146.
84 L. Scarabelli, M. Coronado-Puchau, J. J. Giner-Casares, J. Langer and L. M. Liz-Marzán, *ACS Nano*, 2014, **8**, 5833–5842.
85 L. Scarabelli and L. M. Liz-Marzán, *ACS Nano*, 2021, **15**, 18600–18607.
86 J. E. Millstone, G. S. Métraux and C. A. Mirkin, *Adv. Funct. Mater.*, 2006, **16**, 1209–1214.
87 J. E. Millstone, S. Park, K. L. Shuford, L. D. Qin, G. C. Schatz and C. A. Mirkin, *J. Am. Chem. Soc.*, 2005, **127**, 5312–5313.
88 J. E. Millstone, W. Wei, M. R. Jones, H. J. Yoo and C. A. Mirkin, *Nano Lett.*, 2008, **8**, 2526–2529.
89 P. Choo, D. Arenas-Esteban, I. Jung, W. J. Chang, E. A. Weiss, S. Bals and T. W. Odom, *ACS Nano*, 2022, **16**, 4408–4414.
90 K. Chandra, K. S. B. Culver, S. E. Werner, R. C. Lee and T. W. Odom, *Chem. Mater.*, 2016, **28**, 6763–6769.
91 J. P. Xie, J. Y. Lee and D. I. C. Wang, *Chem. Mater.*, 2007, **19**, 2823–2830.
92 C. L. Nehl, H. W. Liao and J. H. Hafner, *Nano Lett.*, 2006, **6**, 683–688.
93 S. Barbosa, A. Agrawal, L. Rodriguez-Lorenzo, I. Pastoriza-Santos, R. A. Alvarez-Puebla, A. Kornowski, H. Weller and L. M. Liz-Marzán, *Langmuir*, 2010, **26**, 14943–14950.
94 C. Hrelescu, T. K. Sau, A. L. Rogach, F. Jäckel, G. Laurent, L. Douillard and F. Charra, *Nano Lett.*, 2011, **11**, 402–407.
95 A. Indrasekara, S. Meyers, S. Shubeita, L. C. Feldman, T. Gustafsson and L. Fabris, *Nanoscale*, 2014, **6**, 8891–8899.
96 C. G. Khoury and T. Vo-Dinh, *J. Phys. Chem. C*, 2008, **112**, 18849–18859.
97 F. Hao, C. L. Nehl, J. H. Hafner and P. Nordlander, *Nano Lett.*, 2007, **7**, 729–732.
98 S. J. Oldenburg, R. D. Averitt, S. L. Westcott and N. J. Halas, *Chem. Phys. Lett.*, 1998, **288**, 243–247.
99 H. Wang, D. W. Brandl, P. Nordlander and N. J. Halas, *Acc. Chem. Res.*, 2007, **40**, 53–62.
100 E. Prodan, C. Radloff, N. J. Halas and P. Nordlander, *Science*, 2003, **302**, 419–422.
101 H. Wang, Y. P. Wu, B. Lassiter, C. L. Nehl, J. H. Hafner, P. Nordlander and N. J. Halas, *Proc. Natl. Acad. Sci. U. S. A.*, 2006, **103**, 10856–10860.
102 H. Wang, D. W. Brandl, F. Le, P. Nordlander and N. J. Halas, *Nano Lett.*, 2006, **6**, 827–832.
103 X. H. Xia, Y. Wang, A. Ruditskiy and Y. N. Xia, *Adv. Mater.*, 2013, **25**, 6313–6333.
104 A. D. Smigelskas and E. O. Kirkendall, *Trans. Am. Inst. Min., Metall. Pet. Eng.*, 1947, **171**, 130–142.
105 Y. D. Yin, R. M. Rioux, C. K. Erdonmez, S. Hughes, G. A. Somorjai and A. P. Alivisatos, *Science*, 2004, **304**, 711–714.
106 G. G. Li, M. Q. Sun, E. Villarreal, S. Pandey, S. R. Phillpot and H. Wang, *Langmuir*, 2018, **34**, 4340–4350.
107 Y. G. Sun and Y. N. Xia, *J. Am. Chem. Soc.*, 2004, **126**, 3892–3901.
108 Y. G. Sun and Y. N. Xia, *Science*, 2002, **298**, 2176–2179.
109 J. Y. Chen, J. M. McLellan, A. Siekkinen, Y. J. Xiong, Z. Y. Li and Y. N. Xia, *J. Am. Chem. Soc.*, 2006, **128**, 14776–14777.
110 L. Au, Y. C. Chen, F. Zhou, P. H. C. Camargo, B. Lim, Z. Y. Li, D. S. Ginger and Y. N. Xia, *Nano Res.*, 2008, **1**, 441–449.
111 H. Hilal, Q. Zhao, J. Kim, S. Lee, M. Haddadnezhad, S. Yoo, S. Lee, W. Park, W. Park, J. Lee, J. W. Lee, I. Jung and S. Park, *Nat. Commun.*, 2022, **13**, 4813.
112 S. Yoo, J. Lee, H. Hilal, I. Jung, W. Park, J. W. Lee, S. Choi and S. Park, *Nat. Commun.*, 2022, **13**, 4544.
113 M. J. Oh, S. Kwon, S. Lee, I. Jung and S. Park, *ACS Nano*, 2024, **18**, 7656–7665.
114 E. González, J. Arbiol and V. F. Puntes, *Science*, 2011, **334**, 1377–1380.
115 J. Ahn, J. Kim and D. Qin, *Nanoscale*, 2020, **12**, 372–379.
116 G. G. Li, Z. X. Wang and H. Wang, *ChemNanoMat*, 2020, **6**, 998–1013.
117 F. E. M. Issimail, H. Z. You, S. J. Sim and X. Y. Ma, *ACS Nano*, 2025, **19**, 22681–22709.
118 M. B. Cortie and A. M. McDonagh, *Chem. Rev.*, 2011, **111**, 3713–3735.
119 N. E. Motl, A. F. Smith, C. J. DeSantis and S. E. Skrabalak, *Chem. Soc. Rev.*, 2014, **43**, 3823–3834.
120 C. Lemire, R. Meyer, S. Shaikhutdinov and H. J. Freund, *Angew. Chem., Int. Ed.*, 2004, **43**, 118–121.
121 G. C. Bond and D. T. Thompson, *Catal. Rev.: Sci. Eng.*, 1999, **41**, 319–388.
122 A. Abad, P. Concepción, A. Corma and H. García, *Angew. Chem., Int. Ed.*, 2005, **44**, 4066–4069.
123 S. Carrettin, P. Concepción, A. Corma, J. M. L. Nieto and V. F. Puntes, *Angew. Chem., Int. Ed.*, 2004, **43**, 2538–2540.
124 M. Haruta and M. Daté, *Appl. Catal., A*, 2001, **222**, 427–437.
125 I. X. Green, W. J. Tang, M. Neurock and J. T. Yates, *Science*, 2011, **333**, 736–739.
126 Y. He, J. C. Liu, L. L. Luo, Y. G. Wang, J. F. Zhu, Y. G. Du, J. Li, S. X. Mao and C. M. Wang, *Proc. Natl. Acad. Sci. U. S. A.*, 2018, **115**, 7700–7705.
127 J. Biener, M. M. Biener, R. J. Madix and C. M. Friend, *ACS Catal.*, 2015, **5**, 6263–6270.
128 A. Wittstock and M. Bäumer, *Acc. Chem. Res.*, 2014, **47**, 731–739.
129 J. Erlebacher, M. J. Aziz, A. Karma, N. Dimitrov and K. Sieradzki, *Nature*, 2001, **410**, 450–453.
130 Y. Ding, Y. J. Kim and J. Erlebacher, *Adv. Mater.*, 2004, **16**, 1897–1900.
131 A. Wittstock, V. Zielasek, J. Biener, C. M. Friend and M. Bäumer, *Science*, 2010, **327**, 319–322.
132 N. Asao, Y. Ishikawa, N. Hatakeyama, Menggenbateer, Y. Yamamoto, M. W. Chen, W. Zhang and A. Inoue, *Angew. Chem., Int. Ed.*, 2010, **49**, 10093–10095.
133 C. X. Xu, J. X. Su, X. H. Xu, P. P. Liu, H. J. Zhao, F. Tian and Y. Ding, *J. Am. Chem. Soc.*, 2007, **129**, 42–43.
134 V. Zielasek, B. Jürgens, C. Schulz, J. Biener, M. M. Biener, A. V. Hamza and M. Bäumer, *Angew. Chem., Int. Ed.*, 2006, **45**, 8241–8244.
135 T. Fujita, P. F. Guan, K. McKenna, X. Y. Lang, A. Hirata, L. Zhang, T. Tokunaga, S. Arai, Y. Yamamoto, N. Tanaka, Y. Ishikawa, N. Asao, Y. Yamamoto, J. Erlebacher and M. W. Chen, *Nat. Mater.*, 2012, **11**, 775–780.
136 L. V. Moskaleva, S. Röhe, A. Wittstock, V. Zielasek, T. Klüner, K. M. Neyman and M. Bäumer, *Phys. Chem. Chem. Phys.*, 2011, **13**, 4529–4539.
137 Z. W. Quan, Y. X. Wang and J. Y. Fang, *Acc. Chem. Res.*, 2013, **46**, 191–202.
138 Z. Y. Zhou, N. Tian, J. T. Li, I. Broadwell and S. G. Sun, *Chem. Soc. Rev.*, 2011, **40**, 4167–4185.
139 N. Tian, Z. Y. Zhou, S. G. Sun, Y. Ding and Z. L. Wang, *Science*, 2007, **316**, 732–735.
140 Q. F. Zhang and H. Wang, *ACS Catal.*, 2014, **4**, 4027–4033.
141 H. S. Mou, F. Lu, Z. C. Zhuang, Q. W. Chang, L. H. Zhang, X. B. Chen, Y. G. Zhang and J. G. Chen, *Precis. Chem.*, 2024, **2**, 103–111.
142 J. Zhang, M. R. Langille, M. L. Personick, K. Zhang, S. Y. Li and C. A. Mirkin, *J. Am. Chem. Soc.*, 2010, **132**, 14012–14014.
143 F. Lu, Y. Zhang, L. H. Zhang, Y. G. Zhang, J. X. Wang, R. R. Adzic, E. A. Stach and O. Gang, *J. Am. Chem. Soc.*, 2011, **133**, 18074–18077.
144 W. X. Niu, Y. K. Duan, Z. K. Qing, H. J. Huang and X. M. Lu, *J. Am. Chem. Soc.*, 2017, **139**, 5817–5826.

 

145 J. W. Hong, S. U. Lee, Y. W. Lee and S. W. Han, *J. Am. Chem. Soc.*, 2012, **134**, 4565–4568.
146 T. Ming, W. Feng, Q. Tang, F. Wang, L. D. Sun, J. F. Wang and C. H. Yan, *J. Am. Chem. Soc.*, 2009, **131**, 16350–16351.
147 Y. Y. Ma, Q. Kuang, Z. Y. Jiang, Z. X. Xie, R. B. Huang and L. S. Zheng, *Angew. Chem., Int. Ed.*, 2008, **47**, 8901–8904.
148 W. X. Niu, Y. A. A. Chua, W. Q. Zhang, H. J. Huang and X. M. Lu, *J. Am. Chem. Soc.*, 2015, **137**, 10460–10463.
149 Q. F. Zhang, N. Large, P. Nordlander and H. Wang, *J. Phys. Chem. Lett.*, 2014, **5**, 370–374.
150 Q. F. Zhang, N. Large and H. Wang, *ACS Appl. Mater. Interfaces*, 2014, **6**, 17255–17267.
151 E. Villarreal, G. F. G. Li, Q. F. Zhang, X. Q. Fu and H. Wang, *Nano Lett.*, 2017, **17**, 4443–4452.
152 Q. F. Zhang, D. A. Blom and H. Wang, *Chem. Mater.*, 2014, **26**, 5131–5142.
153 M. M. Liang and X. Y. Yan, *Acc. Chem. Res.*, 2019, **52**, 2190–2200.
154 Y. H. Lin, J. S. Ren and X. G. Qu, *Acc. Chem. Res.*, 2014, **47**, 1097–1105.
155 Y. Zhang, E. Villarreal, G. G. Li, W. Wang and H. Wang, *J. Phys. Chem. Lett.*, 2020, **11**, 9321–9328.
156 H. Lim, K. Kani, J. Henzie, T. Nagaura, A. S. Nugraha, M. Iqbal, Y. S. Ok, M. S. A. Hossain, Y. S. Bando, K. C. W. Wu, H. J. Kim, A. E. Rowan, J. Na and Y. Yamauchi, *Nat. Protoc.*, 2020, **15**, 2980–3008.
157 H. Lv, D. D. Xu, J. Henzie, J. Feng, A. Lopes, Y. Yamauchi and B. Liu, *Chem. Sci.*, 2019, **10**, 6423–6430.
158 J. H. Hu, R. B. Jiang, H. Zhang, Y. Z. Guo, J. Wang and J. F. Wang, *Nanoscale*, 2018, **10**, 18473–18481.
159 S. Pedireddy, H. K. Lee, W. W. Tjiu, I. Y. Phang, H. R. Tan, S. Q. Chua, C. Troadec and X. Y. Ling, *Nat. Commun.*, 2014, **5**, 4947.
160 I. McCue, A. Karma and J. Erlebacher, *MRS Bull.*, 2018, **43**, 27–34.
161 G. G. Li and H. Wang, *ChemNanoMat*, 2018, **4**, 897–908.
162 X. Q. Li, Q. Chen, I. McCue, J. Snyder, P. Crozier, J. Erlebacher and K. Sieradzki, *Nano Lett.*, 2014, **14**, 2569–2577.
163 K. Liu, Y. C. Bai, L. Zhang, Z. B. Yang, Q. K. Fan, H. Q. Zheng, Y. D. Yin and C. B. Gao, *Nano Lett.*, 2016, **16**, 3675–3681.
164 G. G. Li, E. Villarreal, Q. F. Zhang, T. T. Zheng, J. J. Zhu and H. Wang, *ACS Appl. Mater. Interfaces*, 2016, **8**, 23920–23931.
165 T. T. Zheng, G. G. Li, F. Zhou, R. Wu, J. J. Zhu and H. Wang, *Adv. Mater.*, 2016, **28**, 8218–8226.
166 G. G. Li, Y. Lin and H. Wang, *Nano Lett.*, 2016, **16**, 7248–7253.
167 G. G. Li, Z. X. Wang, D. A. Blom and H. Wang, *ACS Appl. Mater. Interfaces*, 2019, **11**, 23482–23494.
168 C. J. Murphy, L. B. Thompson, A. M. Alkilany, P. N. Sisco, S. P. Boulos, S. T. Sivapalan, J. A. Yang, D. J. Chernak and J. Y. Huang, *J. Phys. Chem. Lett.*, 2010, **1**, 2867–2875.
169 E. Carbó-Argibay, B. Rodríguez-González, S. Gómez-Graña, A. Guerrero-Martínez, I. Pastoriza-Santos, J. Pérez-Juste and L. M. Liz-Marzán, *Angew. Chem., Int. Ed.*, 2010, **49**, 9397–9400.
170 P. L. Gai and M. A. Harmer, *Nano Lett.*, 2002, **2**, 771–774.
171 B. Goris, S. Bals, W. Van den Broek, E. Carbó-Argibay, S. Gómez-Graña, L. M. Liz-Marzán and G. Van Tendeloo, *Nat. Mater.*, 2012, **11**, 930–935.
172 H. Katz-Boon, C. J. Rossouw, M. Weyland, A. M. Funston, P. Mulvaney and J. Etheridge, *Nano Lett.*, 2011, **11**, 273–278.
173 H. Katz-Boon, M. Walsh, C. Dwyer, P. Mulvaney, A. M. Funston and J. Etheridge, *Nano Lett.*, 2015, **15**, 1635–1641.
174 Z. L. Wang, R. P. Gao, B. Nikoobakht and M. A. El-Sayed, *J. Phys. Chem. B*, 2000, **104**, 5417–5420.
175 X. C. Zhou, N. M. Andoy, G. K. Liu, E. Choudhary, K. S. Han, H. Shen and P. Chen, *Nat. Nanotechnol.*, 2012, **7**, 237–241.
176 Q. F. Zhang, Y. D. Zhou, E. Villarreal, Y. Lin, S. L. Zou and H. Wang, *Nano Lett.*, 2015, **15**, 4161–4169.
177 Q. F. Zhang, L. L. Han, H. Jing, D. A. Blom, Y. Lin, H. L. L. Xing and H. Wang, *ACS Nano*, 2016, **10**, 2960–2974.
178 Q. F. Zhang, H. Jing, G. G. Li, Y. Lin, D. A. Blom and H. Wang, *Chem. Mater.*, 2016, **28**, 2728–2741.
179 L. C. Sun, Q. F. Zhang, G. G. Li, E. Villarreal, X. Q. Fu and H. Wang, *ACS Nano*, 2017, **11**, 3213–3228.
180 I. Lieberman, G. Shemer, T. Fried, E. M. Kosower and G. Markovich, *Angew. Chem., Int. Ed.*, 2008, **47**, 4855–4857.
181 M. L. Nesterov, X. H. Yin, M. Schäferling, H. Giessen and T. Weiss, *ACS Photonics*, 2016, **3**, 578–583.
182 R. Y. Wang, P. Wang, Y. N. Liu, W. J. Zhao, D. W. Zhai, X. H. Hong, Y. L. Ji, X. C. Wu, F. Wang, D. Zhang, W. S. Zhang, R. B. Liu and X. D. Zhang, *J. Phys. Chem. C*, 2014, **118**, 9690–9695.
183 Q. F. Zhang, T. Hernandez, K. W. Smith, S. A. H. Jebeli, A. X. Dai, L. Warning, R. Baiyasi, L. A. McCarthy, H. Guo, D. H. Chen, J. A. Dionne, C. F. Landes and S. Link, *Science*, 2019, **365**, 1475–1478.
184 Y. Zhao, A. N. Askarpour, L. Y. Sun, J. W. Shi, X. Q. Li and A. Alù, *Nat. Commun.*, 2017, **8**, 14180.
185 A. Kuzyk, R. Schreiber, Z. Fan, G. Pardatscher, E.-M. Roller, A. Högele, F. C. Simmel, A. O. Govorov and T. Liedl, *Nature*, 2012, **483**, 311–314.
186 J. Lu, Y. Xue, K. Bernardino, N.-N. Zhang, W. R. Gomes, N. S. Ramesar, S. Liu, Z. Hu, T. Sun, A. F. de Moura, N. A. Kotov and K. Liu, *Science*, 2021, **371**, 1368–1374.
187 M. Wang, J. Dong, C. Zhou, H. Xie, W. Ni, S. Wang, H. Jin and Q. Wang, *ACS Nano*, 2019, **13**, 13702–13708.
188 D. Vila-Liarte, N. A. Kotov and L. M. Liz-Marzán, *Chem. Sci.*, 2022, **13**, 595–610.
189 L. A. Warning, A. R. Miandashti, A. Misiura, C. F. Landes and S. Link, *J. Phys. Chem. C*, 2022, **126**, 2656–2668.
190 X. Shen, C. Song, J. Wang, D. Shi, Z. Wang, N. Liu and B. Ding, *J. Am. Chem. Soc.*, 2012, **134**, 146–149.
191 H.-Y. Ahn, S. Yoo, N. H. Cho, R. M. Kim, H. Kim, J.-H. Huh, S. Lee and K. T. Nam, *Acc. Chem. Res.*, 2019, **52**, 2768–2783.
192 S. W. Im, H.-Y. Ahn, R. M. Kim, N. H. Cho, H. Kim, Y.-C. Lim, H.-E. Lee and K. T. Nam, *Adv. Mater.*, 2020, **32**, 1905758.
193 Y. Wen, M.-Q. He, Y.-L. Yu and J.-H. Wang, *Adv. Coll. Interface Sci.*, 2021, **289**, 102376.
194 H. Kim, S. W. Im, R. M. Kim, N. H. Cho, H.-E. Lee, H.-Y. Ahn and K. T. Nam, *Mater. Adv.*, 2020, **1**, 512–524.
195 Y. M. Yang, L. C. Sun and Q. F. Zhang, *Chin. J. Struct. Chem.*, 2025, **44**, 100467.
196 A. Ben-Moshe, B. Maoz, A. O. Govorov and G. Markovich, *Chem. Soc. Rev.*, 2013, **42**, 7028–7041.
197 Z. L. Cao, H. Gao, M. Qiu, W. Jin, S. Z. Deng, K. Y. Wong and D. Y. Lei, *Adv. Mater.*, 2020, **32**, 1907151.
198 C. Gautier and T. Bürgi, *ChemPhysChem*, 2009, **10**, 483–492.
199 A. Guerrero-Martínez, J. L. Alonso-Gómez, B. Auguié, M. M. Cid and L. M. Liz-Marzán, *Nano Today*, 2011, **6**, 381–400.
200 S. Lee, K. Sim, S. Y. Moon, J. Choi, Y. Jeon, J. M. Nam and S. J. Park, *Adv. Mater.*, 2021, **33**, 2007668.
201 Y. Luo, C. Chi, M. L. Jiang, R. P. Li, S. Zu, Y. Li and Z. Y. Fang, *Adv. Opt. Mater.*, 2017, **5**, 1700040.
202 W. Ma, L. G. Xu, A. F. de Moura, X. L. Wu, H. Kuang, C. L. Xu and N. A. Kotov, *Chem. Rev.*, 2017, **117**, 8041–8093.
203 M. J. Urban, C. Q. Shen, X. T. Kong, C. G. Zhu, A. O. Govorov, Q. B. Wang, M. Hentschel and N. Liu, *Annu. Rev. Phys. Chem.*, 2019, **70**, 275–299.
204 S. L. Wang, X. Liu, S. Mourdikoudis, J. Chen, W. W. Fu, Z. Sofer, Y. Zhang, S. P. Zhang and G. C. Zheng, *ACS Nano*, 2022, **16**, 19789–19809.
205 Z. J. Wang, F. Cheng, T. Winsor and Y. M. Liu, *Nanotechnol.*, 2016, **27**, 412001.
206 L. A. Warning, A. R. Miandashti, L. A. McCarthy, Q. F. Zhang, C. F. Landes and S. Link, *ACS Nano*, 2021, **15**, 15538–15566.
207 W. B. Wu and M. Pauly, *Mater. Adv.*, 2022, **3**, 186–215.
208 L. Sun, Y. Tao, G. Yang, C. Liu, X. Sun and Q. Zhang, *Adv. Mater.*, 2025, **37**, 2306297.
209 C. Brissaud, S. Jain, O. Henrotte, E. Pouget, M. Pauly, A. Naldoni and M. Comesaña-Hermo, *J. Phys. Chem. C*, 2025, **129**, 3361–3373.
210 C. F. McFadden, P. S. Cremer and A. J. Gellman, *Langmuir*, 1996, **12**, 2483–2487.
211 A. Kühnle, T. R. Linderoth and F. Besenbacher, *J. Am. Chem. Soc.*, 2006, **128**, 1076–1077.
212 A. J. Gellman, *Acc. Mater. Res.*, 2021, **2**, 1024–1032.
213 H.-E. Lee, H.-Y. Ahn, J. Mun, Y. Y. Lee, M. Kim, N. H. Cho, K. Chang, W. S. Kim, J. Rho and K. T. Nam, *Nature*, 2018, **556**, 360–365.
214 X. Sun, L. Sun, L. Lin, S. Guo, Y. Yang, B. Zhang, C. Liu, Y. Tao and Q. Zhang, *ACS Nano*, 2024, **18**, 9543–9556.
215 G. González-Rubio, J. Mosquera, V. Kumar, A. Pedrazo-Tardajos, P. Llombart, D. M. Solís, I. Lobato, E. G. Noya, A. Guerrero-Martínez, J. M. Taboada, F. Obelleiro, L. G. MacDowell, S. Bals and L. M. Liz-Marzán, *Science*, 2020, **368**, 1472–1477.

216 J. Chen, X. Gao, Q. Zheng, J. Liu, D. Meng, H. Li, R. Cai, H. Fan, Y. Ji and X. Wu, *ACS Nano*, 2021, **15**, 15114–15122.
217 B. Ni, M. Mychinko, S. Gómez-Graña, J. Morales-Vidal, M. Obelleiro-Liz, W. Heyvaert, D. Vila-Liarte, X. Zhuo, W. Albrecht, G. Zheng, G. González-Rubio, J. M. Taboada, F. Obelleiro, N. López, J. Pérez-Juste, I. Pastoriza-Santos, H. Cölfen, S. Bals and L. M. Liz-Marzán, *Adv. Mater.*, 2023, **35**, 2208299.
218 Y. Ma, Z. Cao, J. Hao, J. Zhou, Z. Yang, Y. Yang and J. Wei, *J. Phys. Chem. C*, 2020, **124**, 24306–24314.
219 S. D. Golze, S. Porcu, C. Zhu, E. Sutter, P. C. Ricci, E. C. Kinzel, R. A. Hughes and S. Neretina, *Nano Lett.*, 2021, **21**, 2919–2925.
220 P. Lyu, R. Espinoza and S. C. Nguyen, *J. Phys. Chem. C*, 2023, **127**, 15685–15698.
221 E. Minutella, F. Schulz and H. Lange, *J. Phys. Chem. Lett.*, 2017, **8**, 4925–4929.
222 A. Lee, S. X. Wu, J. E. Yim, B. Q. Zhao and M. T. Sheldon, *ACS Nano*, 2024, **18**, 19077–19085.
223 A. Sorroche, I. del-Campo, A. Casu, A. Falqui, M. Monge and J. M. López-de-Luzuriaga, *Chem. Commun.*, 2024, **60**, 8204–8207.
224 J. Zhao, S. C. Nguyen, R. Ye, B. H. Ye, H. Weller, G. A. Somorjai, A. P. Alivisatos and F. D. Toste, *ACS Cent. Sci.*, 2017, **3**, 482–488.
225 A. Al-Zubeidi, Y. F. Wang, J. M. Lin, C. Flatebo, C. F. Landes, H. Ren and S. Link, *J. Phys. Chem. Lett.*, 2023, **14**, 5297–5304.
226 Z. L. Mao, H. Vang, A. Garcia, A. Tohti, B. J. Stokes and S. C. Nguyen, *ACS Catal.*, 2019, **9**, 4211–4217.
227 S. K. F. Stofela, O. Kizilkaya, B. T. Diroll, T. R. Leite, M. M. Taheri, D. E. Willis, J. B. Baxter, W. A. Shelton, P. T. Sprunger and K. M. McPeak, *Adv. Mater.*, 2020, **32**, 1906478.
228 M. V. Fonseca Guzman, M. E. King, N. L. Mason, C. S. Sullivan, S. Jeong and M. B. Ross, *Matter*, 2023, **6**, 838–854.
229 C. S. Sullivan, N. L. Mason, A. J. Branco, S. Jeong, O. O. Badru and M. B. Ross, *J. Phys. Chem. C*, 2025, **129**, 11070–11076.
230 M. Q. Sun, A. K. Wang, M. Zhang, S. L. Zou and H. Wang, *ACS Nanosci. Au*, 2024, **4**, 360–373.
231 Y. Chen, Z. X. Fan, Z. M. Luo, X. Z. Liu, Z. C. Lai, B. Li, Y. Zong, L. Gu and H. Zhang, *Adv. Mater.*, 2017, **29**, 1701331.
232 Q. P. Lu, A. L. Wang, Y. Gong, W. Hao, H. F. Cheng, J. Z. Chen, B. Li, N. L. Yang, W. X. Niu, J. Wang, Y. F. Yu, X. Zhang, Y. Chen, Z. X. Fan, X. J. Wu, J. P. Chen, J. Luo, S. Z. Li, L. Gu and H. Zhang, *Nat. Chem.*, 2018, **10**, 456–461.
233 D. Huo, Z. M. Cao, J. Li, M. H. Xie, J. Tao and Y. N. Xia, *Nano Lett.*, 2019, **19**, 3115–3121.
234 C. Martín-Sánchez, A. Sánchez-Iglesias, J. A. Barreda-Argüeso, J. P. Itié, P. Chauvigne, L. M. Liz-Marzán and F. Rodríguez, *Nano Lett.*, 2025, **25**, 3588–3596.
235 S. A. Lee and S. Link, *Acc. Chem. Res.*, 2021, **54**, 1950–1960.
236 A. J. Therrien, M. J. Kale, L. Yuan, C. Zhang, N. J. Halas and P. Christopher, *Faraday Discuss.*, 2019, **214**, 59–72.
237 P. Chatterjee, H. Wang, J. S. Manzano, U. Kanbur, A. D. Sadow and I. I. Slowing, *Catal. Sci. Technol.*, 2022, **12**, 1922–1933.
238 N. Langer and O. Kedem, *J. Phys. Chem. C*, 2022, **126**, 13705–13713.
239 K. Y. Lee, Y. W. Lee, J. H. Lee and S. W. Han, *Colloids Surf., A*, 2010, **372**, 146–150.
240 M. Y. Lin, C. Mochizuki, T. Ishida, Y. Zhang, M. Haruta and T. Murayama, *Catal. Today*, 2023, **410**, 143–149.
241 S. M. Ansar and C. L. Kitchens, *ACS Catal.*, 2016, **6**, 5553–5560.
242 S. Mukherjee, F. Libisch, N. Large, O. Neumann, L. V. Brown, J. Cheng, J. B. Lassiter, E. A. Carter, P. Nordlander and N. J. Halas, *Nano Lett.*, 2013, **13**, 240–247.
243 H. Wang, *Nanophotonics*, 2024, **13**, 4683–4721.
244 H. Wang, *Trends Chem.*, 2024, **6**, 510–524.
245 E. Cortés, L. Besteiro, A. Alabastri, A. Baldi, G. Tagliabue, A. Demetriadou and P. Narang, *ACS Nano*, 2020, **14**, 16202–16219.
246 D. Devasia, A. Das, V. Mohan and P. K. Jain, *Annu. Rev. Phys. Chem.*, 2021, **72**, 423–443.
247 A. Gellé, T. Jin, L. de la Garza, G. D. Price, L. V. Besteiro and A. Moores, *Chem. Rev.*, 2020, **120**, 986–1041.
248 E. Kazuma and Y. Kim, *Angew. Chem., Int. Ed.*, 2019, **58**, 4800–4808.
249 I. Kherbouche, Y. Luo, N. Félidj and C. Mangeney, *Chem. Mater.*, 2020, **32**, 5442–5454.
250 S. Linic, U. Aslam, C. Boerigter and M. Morabito, *Nat. Mater.*, 2015, **14**, 567–576.
251 C. Zhan, X. J. Chen, Y. F. Huang, D. Y. Wu and Z. Q. Tian, *Acc. Chem. Res.*, 2019, **52**, 2784–2792.
252 K. Chen and H. Wang, *Mole. Syst. Des. Eng.*, 2021, **6**, 250–280.
253 L. A. Zhou, D. F. Swearer, C. Zhang, H. Robatjazi, H. Q. Zhao, L. Henderson, L. L. Dong, P. Christopher, E. A. Carter, P. Nordlander and N. J. Halas, *Science*, 2018, **362**, 69–72.
254 G. Baffou, I. Bordacchini, A. Baldi and R. Quidant, *Light: Sci. Appl.*, 2020, **9**, 108.
255 Y. Dubi, I. W. Un and Y. Sivan, *Chem. Sci.*, 2020, **11**, 5017–5027.
256 X. Q. Li, H. O. Everitt and J. Liu, *Nano Res.*, 2020, **13**, 1268–1280.
257 K. X. Chen and H. Wang, *Nano Lett.*, 2023, **23**, 2870–2876.
258 C. Boerigter, U. Aslam and S. Linic, *ACS Nano*, 2016, **10**, 6108–6115.
259 C. Boerigter, R. Campana, M. Morabito and S. Linic, *Nat. Commun.*, 2016, **7**, 10545.
260 B. Seemala, A. J. Therrien, M. H. Lou, K. Li, J. P. Finzel, J. Qi, P. Nordlander and P. Christopher, *ACS Energy Lett.*, 2019, **4**, 1803–1809.

 